

DISPLACEMENT DAMAGE AND IONIZATION EFFECTS IN ADVANCED SILICON-GERMANIUM HETEROJUNCTION BIPOLAR TRANSISTORS

A Thesis
Presented to
The Academic Faculty

by

Akil K. Sutton

In Partial Fulfillment
of the Requirements for the Degree
Master of Science
in Electrical and Computer Engineering

Georgia Institute of Technology
August 2005

DISPLACEMENT DAMAGE AND IONIZATION EFFECTS IN ADVANCED SILICON-GERMANIUM HETEROJUNCTION BIPOLAR TRANSISTORS

Approved by:

Dr. John D. Cressler, Advisor
School of Electrical and Computer Engineering
Georgia Institute of Technology

Dr. Joy Laskar
School of Electrical and Computer Engineering
Georgia Institute of Technology

Dr. David Citrin
School of Electrical and Computer Engineering
Georgia Institute of Technology

Date Approved: July 15, 2005

ACKNOWLEDGEMENTS

First and foremost I would like to thank God who is the source of all my strength. I would like to acknowledge my parents, my brother and many other family members for their continued love, understanding and support during the course of my study.

I would sincerely like to thank Dr. John Cressler for all of his technical guidance and support throughout my masters program. I would like to acknowledge the other members of my thesis advisory committee, Dr. Joy Laskar and Dr. David Citrin, for their support and insightful comments. I would also like to thank my colleagues in the SiGe Devices and Circuits group at Georgia Tech; Becca Haugerud, Ramkumar Krithivasan, Jon Comeau, Dr. A. P. Gnana Prakash, Yuan Lu and Wei-Min Lance Kuo for all their technical assistance and support in the completion of this work.

I am eternally grateful to the SiGe BiCMOS team at IBM Microelectronics for providing the hardware used in these studies. I would also like to thank the following people and agencies for their support of this work: DTRA under the Radiation Hardened Microelectronics Program, NASA-GSFC under the Electronics Radiation Characterization Program, DARPA, and the Georgia Electronic Design Center at Georgia Tech. In addition, the assistance of Paul Marshall, Cheryl Marshall, Robert Reed and Ray Ladbury made the radiation experiments possible and is greatly appreciated.

TABLE OF CONTENTS

	Page
ACKNOWLEDGEMENTS	iii
LIST OF TABLES	vi
LIST OF FIGURES	vii
SUMMARY	x
<u>CHAPTER</u>	
1 SIGE HBT DEVICE PHYSICS AND FABRICATION TECHNIQUES	1
1.1 Introduction	1
1.2 Motivation	1
1.3 SiGe BiCMOS Technology	3
1.3.1 Silicon-Germanium Strained Layer Material Structure	4
1.3.2 Fabrication Techniques – MBE and UHV/CVD	7
1.4 Technology Scaling	9
1.5 Device Operation	13
1.6 Summary	17
2 RADIATION EFFECTS ON ELECTRONIC DEVICES	18
2.1 Introduction	18
2.2 Radiation Environments	18
2.2.1 Particle Types	19
2.2.2 Nomenclature	19
2.2.3 The Space Environment	20
2.3 Displacement Damage	22
2.3.1 Silicon	25

2.3.2 Silicon-Germanium Alloys	26
2.4 Ionization Damage Mechanisms	28
2.4.1 Photon Interaction with Matter	28
2.4.2 Charged Particle Interaction with Matter	32
2.5 Radiation Effects in Bipolar Devices	34
2.6 Summary	35
3 PROTON TOLERANCE OF SIGE HBTS	36
3.1 Introduction	36
3.2 Experiment Design	36
3.2.1 Test Facilities	36
3.2.2 Devices Under Test	37
3.3 dc Results	38
3.4 ac Results	43
3.5 Collector Doping	47
3.6 Summary	50
4 GAMMA AND PROTON DEGRADATION IN SIGE HBTS	52
4.1 Introduction	52
4.2 Experiment Design	52
4.2.1 Devices Under Test	52
4.2.2 Test Facilities	53
4.3 dc Results	53
4.3.1 Technology Scaling and Gamma Degradation	53
4.3.2 Proton vs. Gamma Comparison	56
4.4 Dose Rate Effects	59
4.4.1 Review of Dose Rate Effects for Ionizing Radiation	59

4.4.2 Proton Dose Rate Effects in SiGe HBTs	61
4.5 Damage Factor Extraction	64
4.5.1 Annealing	67
4.5.2 Isothermal Annealing in SiGe HBTs	67
4.6 Summary	71
5 CONCLUSION	72
5.1 Topical Review	72
5.2 Future Direction	73
6 REFERENCES	75

LIST OF TABLES

	Page
Table 1: Material Properties of group IV and III-V elements measured at room temperature (after [13])	4
Table 2: 1 st -, 2 nd -, 3 rd -, and 4 th -generation SiGe HBT performance figures of merit	12
Table 3: Particle masses, charges and radii of interest for radiation effects (after [27])	19
Table 4: Electrical characterization of the dominant radiation defects in Si at 300K (after [28])	25
Table 5: Electrical characterization of the dominant radiation defects in relaxed Si _{1-x} Ge _x epilayers (after [28])	27
Table 6: Incremental dose rate comparison for the proton and gamma irradiation of 200GHz SiGe HBTs	61
Table 7: Forward and inverse gamma displacement damage factors for 120GHz and 200GHz SiGe HBTs	66
Table 8: Forward and inverse mode proton displacement damage factors for 200GHz SiGe HBTs	66

LIST OF FIGURES

	Page
Figure 1: Conceptual representation of the introduction of strain into SiGe lattice structure (after [13])	5
Figure 2: Equilibrium film critical thickness h_{crit} , as a function Ge content x . Experimental and theoretical results are illustrated for various cap layer thicknesses H (after [15])	6
Figure 3: Representative SIMS profile of a 1 st -generation technology with scaling trends indicated by increasing Ge percentage and reduced W_b .	9
Figure 4: Representative cross section of a 1 st -generation SiGe HBT showing locations prone to radiation induced generation/recombination traps	10
Figure 5: Comparison of various SiGe HBT technology nodes in the f_T - f_{max} space (after [22])	11
Figure 6: Representative cross-section of a 4 th -generation SiGe HBT showing locations prone to radiation induced G/R traps (after [25])	12
Figure 7: Ge induced band offsets at the EB and CB junctions resulting from a trapezoidal Ge profile in the p-type SiGe base (after [14]).	13
Figure 8: Gummel characteristics of a Si BJT and SiGe HBT compared showing increased I_C resulting from Ge induced band offsets at the EB junction	15
Figure 9: Solar wind and radiation belts encompassing the Earth (after [29])	21
Figure 10: Displacement effects in a crystal lattice (a) energetic particle creates interstitial-vacancy pair (b) vacancy pair migrates throughout lattice	23
Figure 11: Defects create trap levels in the bandgap that interfere with the dynamics of charge transport via (a) generation, (b) recombination, (c) trapping, (d) compensation and (e) tunneling (after [35])	24
Figure 12: Energy level and structure of intrinsic Si vacancies (after [40]).	26
Figure 13: Competing mechanisms in photon interactions with matter (after [53]).	28
Figure 14: Compton scattering of an incident photon by a quasi free electron (after [27]).	30

Figure 15: Rutherford scattering resulting from the coulombic interaction between an incident particle m_i and target particle M_T (after [27])	33
Figure 16: Creation of oxide and interface trap charge in MOS devices (after [58])	35
Figure 17: 28-pin dip packages used to facilitate in-situ measurement of irradiated samples.	37
Figure 18: 4 th -generation post-radiation forward-mode gummel characteristics showing an increasing $G/R J_B$ and self-annealing after 6 weeks.	39
Figure 19: 4 th -generation post-radiation inverse-mode gummel characteristics showing an increasing $G/R J_B$ and self-annealing after 6 weeks.	39
Figure 20: 4 th -generation post-radiation β characteristics showing a reduction in β_{peak} , but no change in β at peak f_T with proton fluence.	40
Figure 21: β_{peak} degradation as a function of proton fluence for 1 st -, 2 nd -, 3 rd - and 4 th -generation (high and low N_C) devices.	41
Figure 22: Forward-mode I_B degradation for 1 st -, 2 nd -, 3 rd - and 4 th -generation (high and low N_C) devices.	42
Figure 23: Inverse-mode I_B degradation for 1 st -, 2 nd -, 3 rd - and 4 th -generation (high and low N_C) devices.	43
Figure 24: h_{21} extrapolation used to determine f_T for 4 th -generation SiGe HBTs	44
Figure 25: Pre- and post-radiation f_T for 1 st -, 2 nd -, 3 rd - and 4 th -generation SiGe HBTs	45
Figure 26: Pre- and post-radiation f_T and f_{max} for 4 th -generation SiGe HBTs	45
Figure 27: Pre- and post-radiation r_{bb} variation with J_C for 4 th -generation SiGe HBTs	46
Figure 28: The τ_{EC} variation with fluence for 2 nd -, 3 rd - and 4 th -generation SiGe HBTs	47
Figure 29: Extrinsic transconductance for the high- and low-breakdown devices (4 th -generation).	48
Figure 30: Neutral base recombination for the high- and low-breakdown devices (4 th -generation).	49
Figure 31: Forced I_B output characteristics for the high- and low-breakdown devices (4 th -generation).	50
Figure 32: Forward-mode 200GHz SiGe HBT gummel characteristics as a function of cumulative gamma dose	54

Figure 33: Inverse -mode 200GHz SiGe HBT gummel characteristics as a function of cumulative gamma dose	54
Figure 34: Forward-mode excess base current density as a function of gamma dose.	55
Figure 35: Inverse-mode excess base current density as a function of gamma dose.	56
Figure 36: Forward-mode excess base current density for both protons and gamma irradiation in 200GHz SiGe HBTs plotted as a function of equivalent gamma dose.	57
Figure 37: Forward-mode peak current gain degradation for both protons and gamma irradiation in 200GHz SiGe HBTs plotted as a function of equivalent gamma dose	57
Figure 38: Inverse-mode excess base current density for both protons and gamma irradiation in 200GHz SiGe HBTs plotted as a function of equivalent gamma dose.	58
Figure 39: Forward and inverse mode base current density for a 200GHz SiGe HBT showing proton dose rate effects	62
Figure 40: Forward and inverse mode base current for a 200GHz SiGe HBT showing proton dose rate effects	63
Figure 41: Forward mode excess base current for a 200GHz SiGe HBT showing proton dose rate effects compared to standard proton and gamma irradiations	63
Figure 42: Inverse mode excess base current for a 200GHz SiGe HBT showing proton dose rate effects compared to standard proton and gamma irradiations.	64
Figure 43: Forward and inverse mode excess base current density as a function of dose rate for devices of varying emitter areas.	65
Figure 44: Reduction in the forward-mode post radiation base current leakage as a function of anneal time at 300C.	68
Figure 45: Reduction in the inverse-mode post radiation base current leakage as a function of anneal time at 300C.	69
Figure 46: Ratio of the post-anneal base current to post-radiation base current in the forward mode for different annealing time steps at 300C.	70
Figure 47: Ratio of the post-anneal base current to post-radiation base current in the inverse mode for different annealing time steps at 300C.	70

SUMMARY

A summary of total dose effects observed in advanced Silicon Germanium (SiGe) Heterojunction Bipolar Transistors (HBTs) is presented in this work. The principal driving forces behind the increased use of SiGe BiCMOS technology in space based electronics systems are outlined in the motivation section of Chapter I. This is followed by a discussion of the strained layer Si/SiGe material structure and relevant fabrication techniques used in the development of the first generation of this technology. The scaling trends that have enabled the realization of subsequent device generations are also described. Finally a comprehensive description of the device operation is presented, correlating transistor level performance metrics with physical charge transport mechanisms resulting from the incorporation of Ge grading in the base.

Chapter II presents an overview radiation physics as it relates to microelectronic devices. Several sources of radiation are discussed, including the environments encountered by satellites in different orbital paths around the earth. Radiation fields are then described in terms of the nature of their particle types, interaction with matter, damage nomenclature and the radiation induced effects on semiconductor material systems.

Proton irradiation experiments to analyze worst case displacement and ionization damage is examined in chapter III. A description of the test conditions is first presented, followed by the experimental results on the observed variation in the *dc* and *ac* transistor performance metrics with incident radiation. The impact of the collector doping level on the observed degradation levels is also discussed.

In a similar fashion, gamma irradiation experiments to focus on ionization only effects are presented in chapter IV. The experimental design and *dc* results are first

presented, followed by a comparison of degradation under proton irradiation. Additional proton dose rate experiments conducted to further investigate observed differences between proton and gamma results are presented. Additionally, damage factor extractions, geometry considerations and high temperature annealing effects are discussed.

In chapter V future directions for investigation into the total dose response of advanced SiGe HBTs is presented. In particular, areas of interest to be addressed via simulation are outlined. Recommendations are made for other testing that would contribute vastly to the body of knowledge obtained thus far.

CHAPTER I

SIG E HBT DEVICE PHYSICS AND FABRICATION TECHNIQUES

1.1 Introduction

The primary reasons for studying total dose effects in SiGe HBTs are outlined in this chapter. The relevant economic and technological forces at play are first outlined in the motivation section. An overview of the Si/SiGe material system and fabrication techniques are given in the section titled SiGe BiCMOS Technology. Technology scaling is then addressed via industry examples out of the SiGe BiCMOS program at IBM Microelectronics. Finally, in the section entitled device operation, fundamental links are made between the observed performance enhancements and material structure in the device.

1.2 Motivation

Rapid and unprecedented growth in the global telecommunications market continues to pervade all aspects of human life today. According to the Technology Industry Association's 2005 Telecommunications Market Review and Forecast, worldwide telecommunications revenue totaled 2.1 trillion in 2004, up 9.4 percent from 2003 with added growth projected for the period 2004-2008 [1]. Broadband technologies, including DSL, Cable, Satellites, Fixed and Wireless, are at the core of this expansion.

A key enabler of these broadband technologies are the monolithic integrated circuits (ICs) tailored for radio-frequency (RF), microwave and millimeter-wave applications. Among these building blocks are low noise amplifiers (LNA), power

amplifiers (PA), and voltage controlled oscillators (VCO). The fundamental performance metrics of interest for these blocks include low power consumption, high frequency operation and dynamic range, good linearity and low noise. All of these circuit level metrics couple to the device level metrics, and as such understanding these is key to realizing sustained progress in the industry.

One niche market for these ICs is the extra-terrestrial high speed communication links with satellites in orbit around the earth. Operation in this regime encompasses the extreme environments of particle radiation and cryogenic temperatures. These radiation fields result from the magnetosphere and proton and electron belts surrounding the earth. Additionally, solar wind particles trapped in the earth's magnetic field resulting in the 'van Allen' radiation belt are of particular concern for these orbital paths [2, 3]. These harsh environments are responsible for the observed device and circuit performance degradation primarily the result of three mechanisms, namely: (i) displacement damage (DD) effects (ii) ionization damage (iii) and single event effects (SEE). Current trends in technology scaling and advances in fabrication techniques continue to raise questions regarding the reliability of high-speed circuits in these regimes and requires experimental and simulation methods to understand the responses and mitigate component vulnerability.

Silicon-Germanium (SiGe) BiCMOS technology represents the first successful attempt at bandgap engineering in silicon. The end result is a technology that demonstrates performance levels comparable to materials in the exotic III-V world while leveraging an invaluable synergy with traditional low-cost, high yield Si CMOS manufacturing [4]. SiGe BiCMOS technology continues to remain a formidable contender for space-based communications applications based on its robust tolerance to high levels of TID and DD effects [5]. The technology is however somewhat less robust to SEE, and wide variety of circuit architectures have been implemented to address "hardening by design" concepts [6] to enable increased tolerance with minimal change to fabrication modules.

The primary goal of this thesis will be to provide insight into the DD and TID mechanisms present in advanced SiGe HBTs. Proton and gamma irradiation experiments are used simulate the accumulated dose an electronic part may see in a given orbital mission. Transistor level *dc* and *ac* measurements are employed to observe the induced effects. Special consideration is given to novel device structures, collector doping levels and device geometry, dose rate effects and high temperature annealing.

1.3 SiGe BiCMOS Technology

Germanium has long been identified as a suitable material for semiconductor device design primarily on account of its high electron mobility $\mu_{n,Ge} \approx 3500 \text{cm}^2/\text{V} - \text{sec}$, $\mu_{n,Si} \approx 1350 \text{cm}^2/\text{V} - \text{sec}$ for $T = 300\text{K}$, $N_{A,D} = 10^{16} \text{cm}^{-3}$ [7]. It is no secret however that silicon is by far cheaper, easier to process, and much more abundant and hence is at the core of the trillion dollar semiconductor industry. Moreover, the idea of combining silicon and germanium to leverage desirable electrical characteristics in a bipolar transistor is not new, having been originally proposed by Shockley back in 1950 [4]. It was not until the 1990's however, that advances in ultra high vacuum / chemical vapor deposition (*UHV/CVD*) techniques enabled the realization of device quality, epitaxial SiGe films at a much lower Dt than was previously possible with conventional high temperature Si-based epitaxy. This resulted in films with better dopant confinement and reduced out-diffusion [8]. The functional dependence of dopant diffusion on process temperature and time is captured via Fick's second law, outlined in Equation 1 [9].

$$\frac{\partial C}{\partial t} = D \nabla^2 C \quad (1)$$

Using Fair's vacancy model for silicon the diffusion coefficient is given in Equation 2.

$$D = D^o + \frac{n}{n_i} D^- + \left[\frac{n}{n_i} \right]^2 D^{2-} + \left[\frac{n}{n_i} \right]^3 D^{3-} + \dots + \frac{p}{n_i} D^+ + \left[\frac{p}{n_i} \right]^2 D^{2+} + \left[\frac{p}{n_i} \right]^3 D^{3+} \quad (2)$$

Table 1: Material properties of group IV and III-V elements measured at room temperature (after [13]).

Material	$E_g(eV)$	$\mu_n(cm^2/Vs)$	$\mu_p(cm^2/Vs)$	$a(A)$	$\rho(g/cm^3)$	$Melting(C)$
<i>Si</i>	1.12	1350	480	5.43	2.33	1415
<i>Ge</i>	0.67	3900	1900	5.66	5.32	936
<i>GaAs</i>	1.43	8500	400	5.65	5.31	1238
<i>InP</i>	1.34	4000	100	6.06	4.79	1070

The temperature dependence is accounted for via the arrhenius relationship shown in Equation 3.

$$D^o = D_o^o e^{-E_a^o/kT} \quad (3)$$

Almost two decades following the realization of device quality SiGe films, process maturation has resulted in a Silicon-Germanium (SiGe) BiCMOS technology that is currently in fabrication at over 40 commercial foundries worldwide. The end result is a technology that demonstrates performance levels comparable to materials in the exotic III-V world while leveraging an invaluable synergy with traditional low-cost, high yield Si CMOS manufacturing [4].

1.3.1 Silicon-Germanium Strained Layer Material Structure

In stark contrast to the AlGaAs material system, Si and Ge have quite different lattice constants which pose signifiant challenges for the fabrication of device quality films as shown in Table 1. The lattice constants for Si and Ge (a_{Si} and a_{Ge}) can be used to calculate a SiGe lattice constant ($a_{Si_{1-x}Ge_x}(x)$) according to Vegard's rule Equation 4 and has been verified experimentally [10, 11, 12]. The corresponding lattice constant mismatch $f_m(x)$ is calculated to be 0.042 for the values in Table 1.

$$a_{Si_{1-x}Ge_x}(x) = a_{Si} + (a_{Ge} - a_{Si})x \quad f_m(x) = \frac{a_{Si_{1-x}Ge_x}(x) - a_{Si}}{a_{Si}} = 0.042x \quad (4)$$

A pictorial representation of the strain inherent to the SiGe layer epitaxially grown on a Si substrate is illustrated in Figure 1. An additional unstrained Si buffer and cap (thickness H) layers are inserted below and above the strained SiGe (thickness

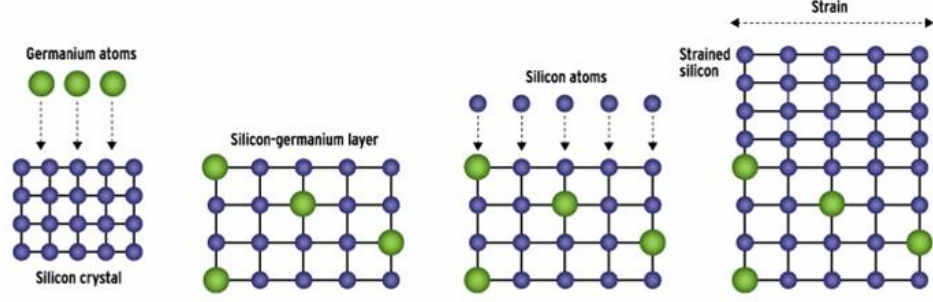


Figure 1: Conceptual representation of the introduction of strain into SiGe lattice structure (after [13]).

h) layer respectively. The presence of $f_m(x)$ between Si and Ge necessarily means that in order for a contiguous, defect free, device quality film to exist at the $Si/SiGe$ interface the epitaxial $SiGe$ layer must be biaxially compressed. The resulting strain energy stored in the system (E_H) is given in Equation 5 [14].

$$E_H = B f_m^2 h \text{ where } B = 2\mu \frac{1+\nu}{1-\nu}, f_m = \text{misfit strain}, h = \text{epilayer thickness} \quad (5)$$

The inherent strain energy in the system, necessarily constrains the thickness (h) to which the SiGe epilayer can be grown. Thermodynamic stability theory dictates that there exist a critical thickness (h_{crit}) above which the film is unstable and can spontaneously relax subsequently leading to defect formation via thermal processing steps for example. h_{crit} strongly depends on the Ge content (x) as determined by the Matthews and Blakeslee result shown in Equation 6. The effect of the cap layer thickness H on the observed stability profile is captured in Figure 2.

$$x = \frac{b \cos \lambda}{0.084 h_{crit}} \left[\gamma + \frac{1 - \frac{\nu}{4}}{4\pi \cos^2 \lambda \cos \phi (1 + \nu)} \left[\ln \frac{h_{crit} + H}{b} + \delta \ln \frac{H}{b} - \delta \ln \frac{1}{\gamma} \right] \right] \quad (6)$$

In the above expression b is the magnitude of the Burger's vector, λ is the angle between the Burger's vector and the interface normal to the dislocation line, ϕ is the angle between the slip plane and the normal vectors to the strained interface, ν is a parametric constant and δ and γ are given by $\delta = \frac{H}{h_{crit} + H}$ and $\gamma = \frac{h_{crit}}{h_{crit} + H}$. To be sure, the Ge content, plotted in Figure 2 is the average Ge fraction given by

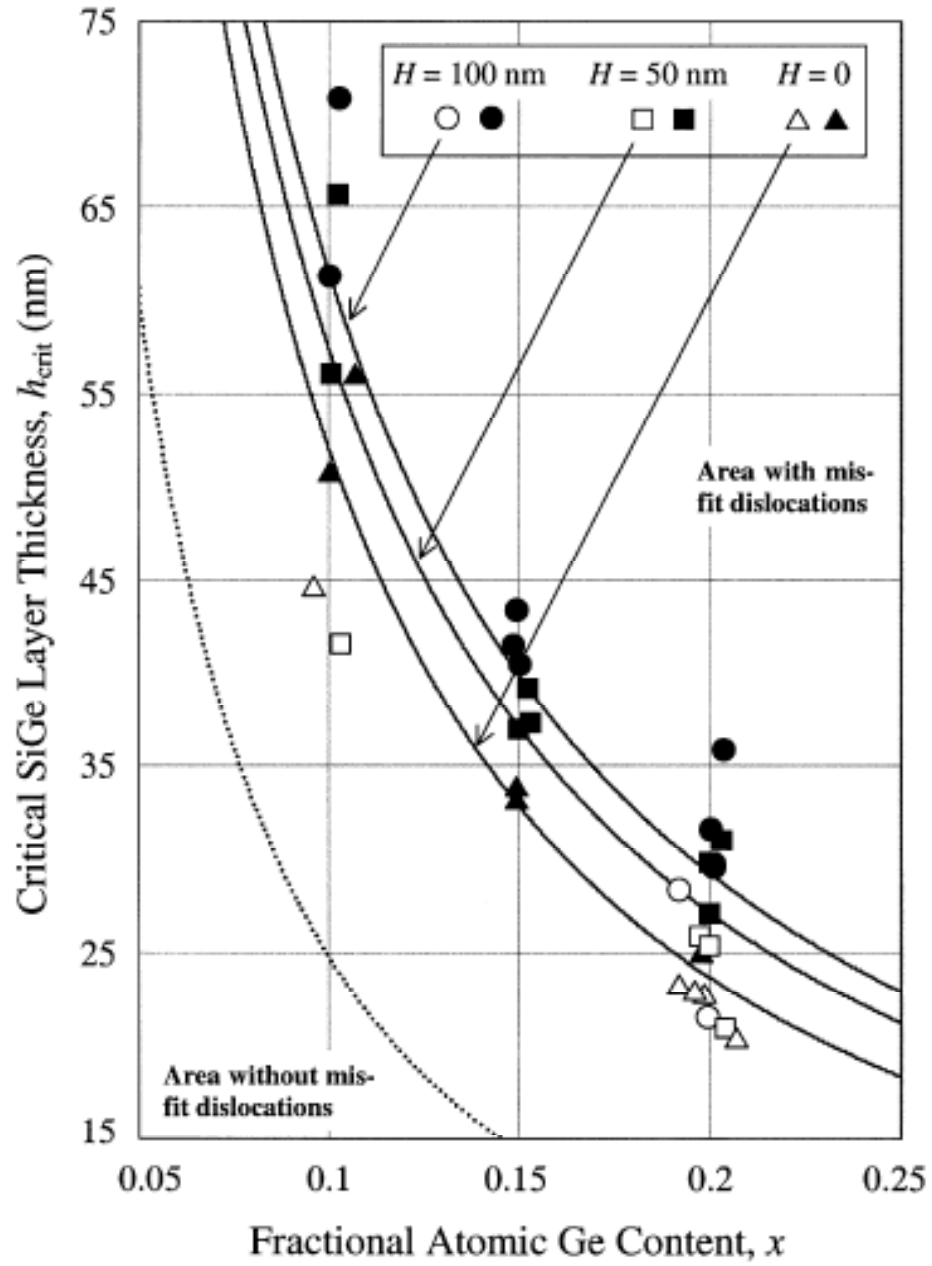


Figure 2: Equilibrium film critical thickness h_{crit} , as a function of Ge content x . Experimental and theoretical results are illustrated for various cap layer thickness H (after [15]).

$\bar{x} = \frac{1}{h} \int_0^h x(z) dz$, where x is a function of the vertical depth z into the profile (known as the Ge grading).

1.3.2 Fabrication Techniques - MBE and UHV/CVD

The realization of device quality films in the Si/SiGe material system are critically dependant on the presence of a pristine growth interface and precise dopant control. There are a myriad of fabrication techniques tailored to control the introduction of dopant atoms into a bulk semiconductor material. Traditional CMOS processing has relied on furnace doping, diffusion and ion implantation to selectively introduce impurity crystals into the host lattice structure. These processes are highly unsuitable for strained layer film processing since they introduce defects into the crystal lattice or subject it to additional Dt steps.

Epitaxy has long been employed as a growth technique for stacking crystalline layers of different crystal orientation yet maintaining a constant lattice constant at the interface. Dopant species can be selectively introduced as the film is grown, thereby resulting in increased control over the placement of localized impurity traps. In its formative years, epitaxial growth was done primarily using chemical vapor deposition (CVD) techniques. CVD epitaxy, however, is particularly suited for films in excess of $20\mu m$ and is typically processed at temperatures in excess of $1200C$ [16].

Molecular Beam Epitaxy (MBE) is an older technique developed in the 1960's as an alternative to CVD epitaxy. MBE is more suitable for SiGe strained layer growth on account of its lower operating temperatures and capability to produce reliable thin films. To be sure, MBE reactors typically operate under pressures of $10^{-10} Torr$ and at temperatures centered at $800C$ [16]. Typical MBE processes implement a high vacuum evaporation of constituent precursors and the necessary dopant to be incorporated into the final film structure. The species are adsorbed onto the surface and diffuse through until their final energy relegates them to adopt a compliant position within host crystalline lattice [16]. The low temperature

operation of MBE makes it particularly apt for strained layer film processing.

Ultra High Vacuum Chemical Vapor Deposition (UHV/CVD) combines many of the advantages of MBE with novel cleaning methods not previously realized in older CVD techniques. The operating temperature of a typical UHV CVD reactor is centered at 500C, substantially lower than any of its predecessors. The thermodynamic volatility of the strained layer system prescribes that the thermal budget of subsequent processing be made as conservative as possible. The near pristine conditions of the UHV setup are the principle driving force behind the significantly reduced contamination levels along Si/SiGe interfaces. In particular, the final HF termination step, used to create a hydrophobic surface, eliminated the need for intermediate cleaning steps during film growth thereby dramatically reducing contamination levels of trace elements during processing.

UHV/CVD also exhibits remarkable control over the impurity dopant profiles in the active base region, demonstrating that a variation in the content of gas phase impurity species with time could be correlated with the spatial concentration of the given species in the epitaxial film. Growth rate is an important metric of interest for any epitaxial process. An interesting result of the UHV/CVD process was that the growth rate of the strained layer film could be modulated by the actual Ge percentage in the gas phase content [17]. The implications for manufacturing are positive. It has already been shown that increased Ge percentage bears a positive correlation with the minimum possible SiGe film thickness [18]. This result, combined with the UHV/CVD growth characteristics, imply that thinner films can be grown faster and at a more controlled rate using UHV/CVD. Furthermore, the precision of the growth system can then be further tailored by adjusting the Ge percentage content in the film nearing the endpoint of the reaction and using in-situ measurement techniques to confirm desired film thickness.

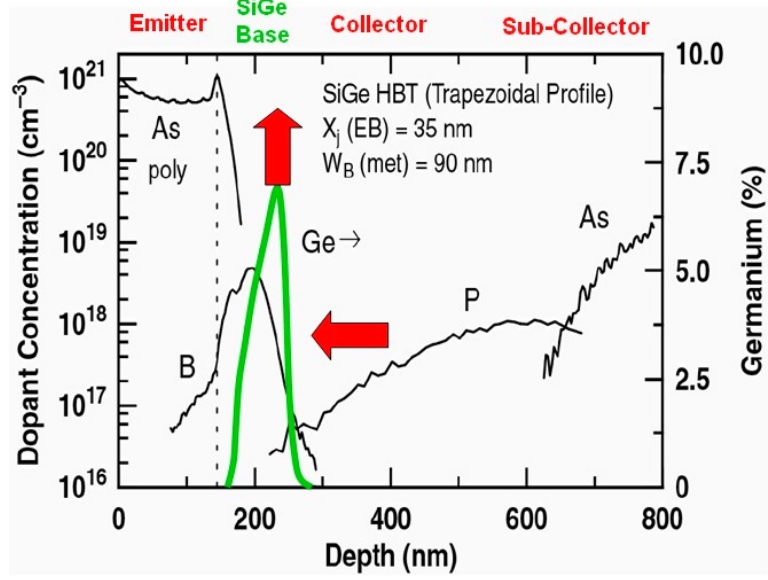


Figure 3: Representative SIMS profile of a 1st-generation technology with scaling trends indicated by increasing Ge percentage and reduced W_b .

1.4 Technology Scaling

For the purposes of illustrating technology scaling in advanced bipolar processes industry examples from IBM Microelectronics are used. The teams at IBM Microelectronics have arguably been the first to realize SiGe HBT devices and their work enables a comprehensive look at the trends in the scaling of the technology over more than a decade with four distinct generations in production to date. The increased switching speed resulting from continued reduction in minimum CMOS feature size (in keeping with Moore's Law) is matched by corresponding increases in peak cutoff frequency (f_T) attained through vertical profile scaling and increased dopant concentration on the bipolar side. This is illustrated in in Figure 3 which depicts the representative Secondary Ion Mass Spectroscopy (SIMS) profile of a 1st-generation device. Scaling trends including reduction in the neutral base width W_B and increased peak Ge fraction x are also illustrated.

The 1st generation SiGe HBTs (IBM 5HP), achieved a peak f_T of 50GHz, and was manufactured in a 0.5 μ m CMOS compatible technology with a collector-emitter breakdown voltage (BV_{CEO}) of 3.3V [19]. A representative cross section of this

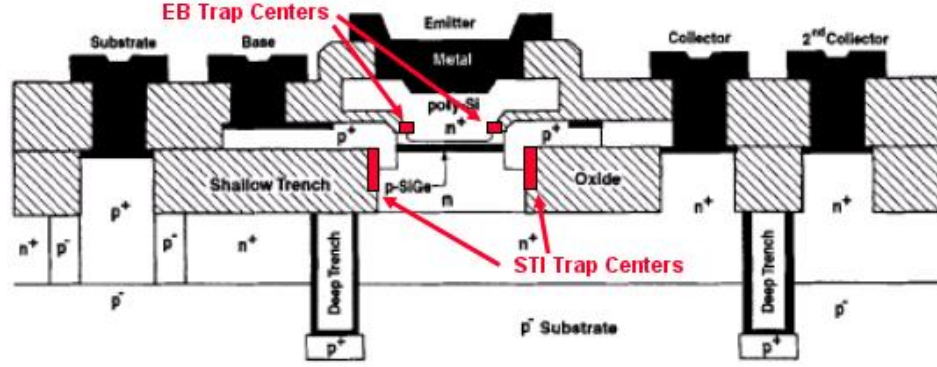


Figure 4: Representative cross-section of a 1st-generation SiGe HBT showing locations prone to radiation induced generation / recombination traps.

technology is illustrated in Figure 4 with the areas prone to radiation induced trap formation highlighted.

The important characteristics of the device cross section are now described [4]. The device is built on an $n+$ subcollector ($5-10\Omega/\text{sq}$) on a $p-$ substrate ($10-15\Omega\text{-cm}$) with a lightly doped epitaxial n -type collector. Poly-silicon deep trenches are used to isolate adjacent devices, and shallow trench oxides are used for internal isolation. The base is formed through the growth of a composite SiGe epitaxial layer composed of a Si buffer ($10-20\text{nm}$), a boron doped active layer ($70-100\text{nm}$), and a final Si cap ($10-30\text{nm}$). Within the base region, there is trapezoidal Ge graded profile. A selectively implanted collector (SIC) $1 \times 10^{17}\text{cm}^{-3}$ (phosphorus) is used to reach the subcollector and to reduce collector resistance (R_C). The emitter is heavily doped with arsenic ($1 \times 10^{21}\text{cm}^{-3}$), and is fully self-aligned to the base using an emitter base (EB) spacer. A polysilicon extrinsic base and silicided intrinsic base ($5-10\Omega/\text{sq}$) facilitates transistor contacts to the back end metallization. IBM 5HP featured a nominal emitter width W_E , of $0.5\mu\text{m}^2$, while in the 2nd-generation device (IBM 7HP), lateral and vertical scaling methodologies were employed to realize nominal linewidths of $W_E = 0.2\mu\text{m}^2$ [20].

The 4th-generation SiGe HBTs (IBM 9T) achieve a remarkable peak f_T of 350

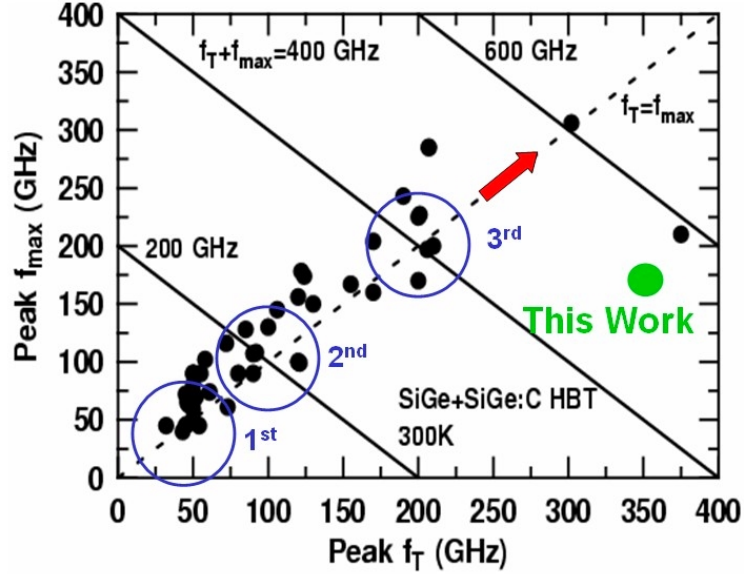


Figure 5: Comparison of various SiGe HBT technology nodes in the f_T - f_{max} space (after [22]).

GHz. This is a record for any Si-based transistor. This unprecedented level of frequency response represents a 67% increase over the previous performance record, and was fabricated in a 120 nm, 100% Si-compatible technology. The details of the device design and performance are detailed in [21]. Process windows currently enable the realization of peak f_T and f_{max} both above 300GHz through careful optimization, as recently reported in [22]. Most recently, a simultaneous f_T and f_{max} of 350/300 GHz has been reported [23]. There is tremendous leverage in the f_T and f_{max} design space even as the technology pushes to higher frequencies as is illustrated in Figure 5. The associated collector-emitter (BV_{CEO}) and collector-base (BV_{CBO}) breakdown voltages are 1.4V and 5.0V, respectively, yielding an $f_T \times BV_{CEO}$ product well above the 200GHzV "Johnson limit" [24]. In the 3rd-generation SiGe HBT (IBM 8HP), an improvement in peak f_T , to 200GHz, was realized only through fundamental changes in the physical structure of the transistor. Specifically, a reduced thermal cycle, "raised extrinsic base" structure was implemented using conventional deep and shallow trench isolation (STI), in addition to an *in-situ* doped polysilicon emitter. The SiGe base region features an

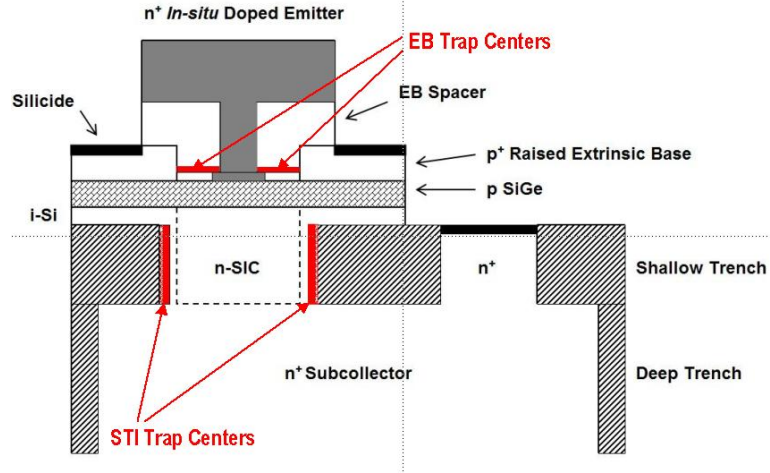


Figure 6: Representative cross-section of a 4th-generation SiGe HBT showing locations prone to radiation induced G/R traps after [25].

Table 2: 1st-, 2nd-, 3rd-, and 4th-generation SiGe HBT performance Figures of merit.

Figure of Merit	1 st (5HP)	2 nd (7HP)	3 rd (8HP)	4 th (9T)
Actual W_E (μm)	0.42	0.18	0.12	0.12
peak f_T (GHz)	50	120	207	300
peak f_{max} (GHz)	70	100	285	170
BV_{CEO} (V)	3.3	2.5	1.7	1.4

unconditionally stable, 25% peak Ge, C-doped profile deposited using UHV/CVD epitaxial growth techniques as described in [25]. A representative cross section of this new structure is depicted in Figure 6. The key performance metrics for the 1st- through 4th-generation SiGe HBT devices are illustrated in Table 2.

In the case of the new 4th-generation technology (same representative cross-section as for the 3rd-generation technology), performance enhancements were realized primarily through careful profile optimization and aggressive vertical scaling of the base and collector regions, resulting in a record emitter-to-collector transit time (τ_{EC}) of 0.45 psec [21]. The key fabrication parameters that were adjusted to realize such performance include the base width (W_B), Ge content, and dopant profiles as highlighted in the representative SIMS doping profile illustrated in Figure 3.

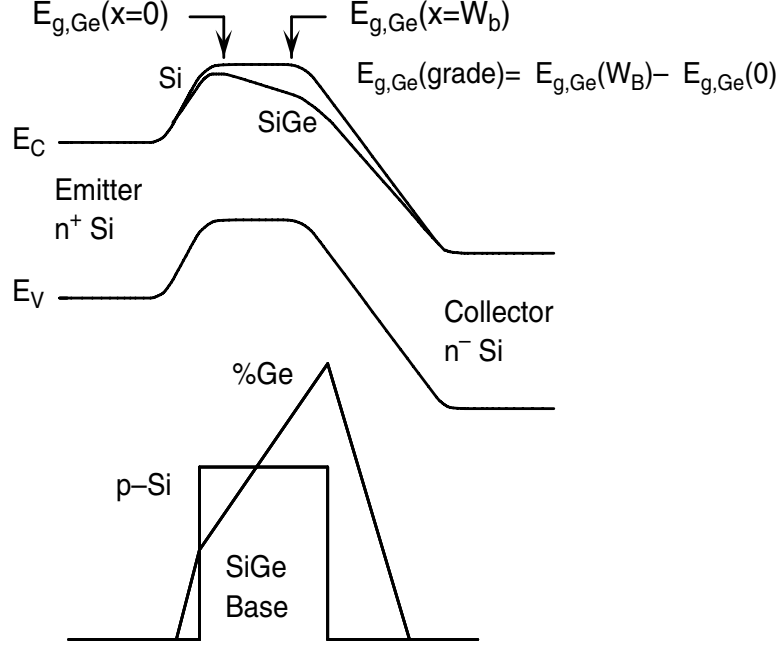


Figure 7: *Ge* induced band offsets at the EB and CB junctions resulting from a trapezoidal *Ge* profile in the p-type SiGe base after [4].

1.5 Device Operation

The fundamental physical mechanisms for the operation of the SiGe HBT are now presented following the discussion in [4] and references therein.

The inclusion of the graded *Ge* profile in the boron-doped p-type base of the SiGe HBT effectively creates a strained lattice structure in the base according to the Vegard's rule (for $Si_{1-x}Ge_x$) as shown in Equation 4. This strain is effectively translated into a *Ge* induced offset in the bandgap (E_g) both at the EB [$\Delta E_{g,Ge}(x = 0)$] and CB [$\Delta E_{g,Ge}(x = W_b)$] junctions of the device as illustrated in Figure 7. Moreover, since the *Ge* is graded across the width of the neutral base, the differences in band offsets translates into a an additional *Ge* induced drift-field ($(\Delta E_{g,Ge}(x = W_b) - \Delta E_{g,Ge}(x = 0))/W_b$) resulting in a further acceleration of the minority carriers in the base, thereby improving the frequency response of the device. Additionally, [$\Delta E_{g,Ge}(x = 0)$] effectively translates into a lower barrier for electrons being injected from the emitter into the base. Then for the same applied

base-emitter voltage (V_{BE}), there is exponentially more electron injection, translating into larger collector current (I_C), and current gain (β), for the same base current (I_B). This provides significantly more leverage in circuit design applications over conventional Si BJTs.

The expression for the collector current density ($J_C = I_C/A_E$) is obtained using the Moll-Ross relations [26], valid for low injection, fixed V_{BE} , and temperature (T) shown in Equation 7.

$$J_C = \frac{q \left(e^{qV_{BE}/kT} - 1 \right)}{\int_0^{W_b} \frac{p_b(x)dx}{D_{nb}(x)n_{ib}^2(x)}} \quad (7)$$

The effects of the Ge induced band-offsets are coupled into this expression through the intrinsic carrier density ($n_{ib}^2(x)$) and carrier diffusivity (D_{nb}). $n_{ib}^2(x)$ is given in Equation 8 where the position dependant bandgap narrowing factor is described in Equation 9.

$$n_{ib}^2(x) = (N_C N_V)_{SiGe}(x) e^{-E_{gb}(x)/kT} \quad (8)$$

$$E_{gb}(x) = E_{gbo} - \Delta E_{gb}^{app} + [\Delta E_{g,Ge}(0) - \Delta E_{g,Ge}(W_b)] \frac{x}{W_b} - \Delta E_{g,Ge}(0) \quad (9)$$

E_{gb}^{app} is the apparent heavy doping bandgap narrowing in the base region, and E_{gbo} is the bandgap of Si under low-doping (i.e. 1.12eV). An additional useful parameter is the % Ge grading across the base defined in Equation 10.

$$\Delta E_{g,Ge}(grade) = \Delta E_{g,Ge}(W_b) - \Delta E_{g,Ge}(0) \quad (10)$$

$$J_C = \frac{qD_{nb}}{N_{ab}^- W_b} \left(e^{qV_{BE}/kT} - 1 \right) n_{io}^2 e^{\Delta E_{gb}^{app}/kT} \left\{ \frac{\tilde{y}\tilde{\eta}\Delta E_{g,Ge}(grade)/kT e^{\Delta E_{g,Ge}(0)/kT}}{1 - e^{-\Delta E_{g,Ge}(grade)/kT}} \right\} \quad (11)$$

The final expression for J_C in a SiGe HBT is then given by Equation 11 where \tilde{y} and $\tilde{\eta}$ represent the effective density of states ratio ($SiGe/Si$) and the minority carrier diffusivity ratio ($SiGe/Si$) respectively. It can easily be seen that J_C is then dominated by the $[\Delta E_{g,Ge}(x=0)]$ term in the exponent of the numerator. As previously stated, this band offset at the EB junction exponentially increases the number of electrons injected into the base. The improved $J_{C,SiGe}$ compared to $J_{C,SiGe}$ is clearly depicted in Figure 8

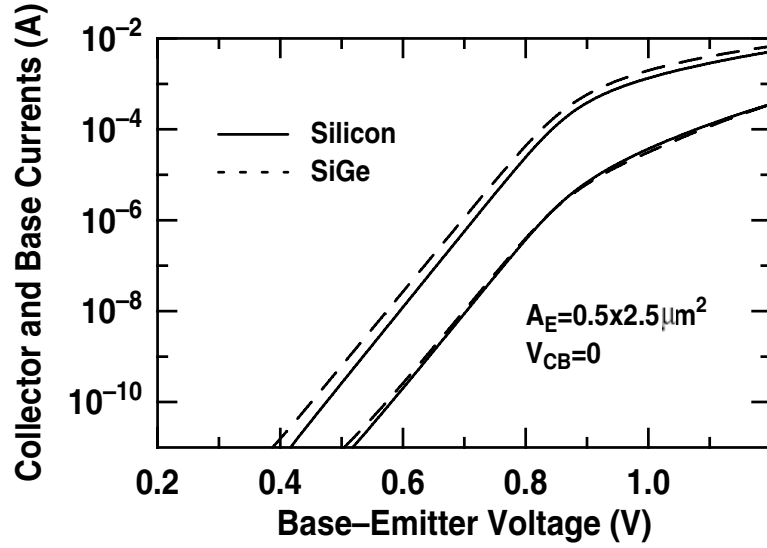


Figure 8: Gummel characteristics of a Si BJT and SiGe HBT compared showing increased I_C resulting from Ge induced band offsets at the EB junction.

Assuming that the SiGe HBT and Si BJT are similarly constructed, with comparable J_B the enhancement in current gain (Ξ) at fixed V_{BE} is described by Equation 12. As with J_C , Ξ exhibits an exponential dependence on $\Delta E_{g,Ge}(x=0)$, but a linear dependence on $\Delta E_{g,Ge}(grade)$. This implies that a "box" profile is most suitable to exploit enhancements in Ξ . Additionally, since T is incorporated in the denominator of the exponent these enhancements are further improved at cryogenic temperatures.

$$\left. \frac{\beta_{SiGe}}{\beta_{Si}} \right|_{V_{BE}} = \Xi = \left[\frac{\tilde{y}\tilde{\eta}\Delta E_{g,Ge}(grade)/kT e^{\Delta E_{g,Ge}(0)/kT}}{1 - e^{-\Delta E_{g,Ge}(grade)/kT}} \right] \quad (12)$$

To be sure, the Ge profile can be tuned to match other parameters such as the Early Voltage (V_A), emitter and base transit times (τ_e and τ_b) and cutoff frequency (f_T). Using the definition for V_A outlined in Equation 13 and making the relevant substitutions according to the Moll-Ross relations in Equation 7 yields the Ge profile dependent expression for the V_A enhancement in a SiGe HBT shown in Equation 14.

$$V_A = J_C(0) \left\{ \left. \frac{\partial J_C}{\partial V_{CB}} \right|_{V_{BE}} \right\}^{-1} \simeq J_C(0) \left\{ \left. \frac{\partial J_C}{\partial W_b} \right|_{V_{BE}} \frac{\partial W_b}{\partial V_{CB}} \right\}^{-1} \quad (13)$$

$$\left. \frac{V_{A,SiGe}}{V_{A,Si}} \right|_{V_{BE}} \simeq \frac{e^{\Delta E_{g,Ge}(grade)/kT}}{\Delta E_{g,Ge}(grade)/kT} \quad (14)$$

The dynamics of carrier transport, especially as it relates to the high frequency operation of the device is dominated by the parameters τ_e, τ_b, f_T . The Moll-Ross base transit time equations at low-injection is given in Equation 15.

$$\tau_b = \int_0^{W_b} \frac{n_{ib}^2(x)}{p_b(x)} \left[\int_0^{W_b} \frac{p_b(y)dy}{D_{nb}(y)n_{ib}^2(y)} \right] dx \quad (15)$$

Utilizing the expression for n_{ib}^2 given in Equation 8 and making the relevant substitutions and simplifications yields the corresponding relationship for a SiGe HBT as given in Equation 16.

$$\tau_{b,SiGe} = \frac{W_b^2}{\tilde{D}_{nb}} \frac{kT}{\Delta E_{g,Ge}(grade)} \left\{ 1 - \frac{(1 - e^{-\Delta E_{g,Ge}(grade)/kT}) kT}{\Delta E_{g,Ge}(grade)} \right\} \quad (16)$$

Under the assumptions of constant base doping and bandgap, Equation 15 can be simplified for a Si BJT to yield base transit time $\tau_{b,Si} = \frac{W_b^2}{2D_{nb}}$. The resultant Ge induced transit time enhancement is equivalent to Equation 16 with the exception that $\frac{W_b^2}{\tilde{D}_{nb}}$ is replaced by a factor $\frac{2}{\tilde{\eta}}$. The emitter transit time enhancement is determined in a similar fashion and is given in Equation 17.

$$\frac{\tau_{e,SiGe}}{\tau_{e,Si}} \simeq \frac{J_{C,Si}}{J_{C,SiGe}} = \frac{1 - e^{-\Delta E_{g,Ge}(grade)/kT}}{\tilde{\gamma}\tilde{\eta} \frac{\Delta E_{g,Ge}(grade)}{kT} e^{\Delta E_{g,Ge}(0)/kT}} \quad (17)$$

The implications of the expressions is simply that one can tailor the Ge profile in the base to optimize different performance Figures merit. Box profiles with large $\Delta E_{g,Ge}(x=0)$ are suitable for β enhancement. Strong $\Delta E_{g,Ge}(grade)$, or large $\Delta E_{g,Ge}(x=W_b)$ yield improved V_A , τ_e , τ_b and hence f_T .

Advanced SiGe HBT profiles, such as the ones under investigation in this work, employ trapezoidal profiles in an attempt to achieve simultaneously good β and $J_{C,SiGe}$ as well as V_A and f_T . The success of this approach is evidenced in [22] with IBM 9T devices with $f_T \times BV_{CEO}$ products well above the Johnson Limit [24]. The effects of radiation on semiconductor materials, and on SiGe HBTs in general is considered next.

1.6 Summary

A substantial body of evidence has been presented in support of the study of radiation effects in advanced SiGe HBTs. In particular, the increasing value of SiGe BiCMOS technology to the space communication market has been demonstrated. The salient features of the SiGe material system have been explored and the path to realization of device quality films has been tracked. Novel techniques employed to realize performance enhancements in the technology have been discussed. Finally, an in depth discussion on the fundamental features of the device operation has been presented with explicit correlations between the base Ge profile and metrics such as β , f_T , BV_{CEO} and V_A .

CHAPTER II

RADIATION EFFECTS ON ELECTRONIC DEVICES

2.1 Introduction

This chapter will examine the relevant physical mechanisms behind the interaction of radiation with matter, and in particular the effect of radiation on semiconductor material systems. The first section will discuss the radiation environments that may be encountered by microelectronic circuits. The next section will discuss the interaction of ionizing radiation with matter. Particular emphasis will be placed on gamma radiation and heavy charged particles. Specific radiation effects in bipolar technologies is considered next with examples from the literature. In addition several of the key features of displacement damage and ionization effects in these technologies are described.

2.2 Radiation Environments

Microelectronic devices and circuits are routinely used in a variety of radiation intense environments. Common examples include: (i) a variety of diagnostic equipment used for radiology in the health sector, (ii) control systems in nuclear power plants in the energy sector (iii) high energy particle physics experiments, (iv) the natural environment, (v) semiconductor processing modules such as ion implantation, plasma deposition and etch and (vi) Extra-terrestrial applications such as commercial and military satellites in the defense sector. The next two sections itemize the particles of primary concern in addition to giving additional insight into the radiation fields comprising the space environment.

Table 3: Particle masses, charges and radii of interest for radiation effects after [27].

Particle Type	Mass(kg)	Charge(C)	Radius (m)
Proton	1.672×10^{-27}	1.602×10^{-19}	1.535×10^{-18}
Neutron	1.674×10^{-27}	0	6.317×10^{-18}
Electron	9.109×10^{-31}	1.602×10^{-19}	2.817×10^{-15}

2.2.1 Particle Types

The constituent particles that compose the radiation fields previously described can be classified as either photons, charged particles or neutrons. Photons can refer to either x - or γ -rays from the electromagnetic spectrum. Charged particles include electrons, protons, neutrons, α - particles and heavy ions. A summary of the properties of interest for some particles are illustrated in Table 3. The exact interaction mechanism between the described particles and the target material depends on several factors. The mass (m_p), charge (q_p), and kinetic energy (KE_p) of the incident particle along with the atomic number (Z_T), charge (q_T), and density (ρ_T) of the target atoms are all critical to the determination of the most energetically favorable reaction. For example, Photons are capable of interacting with the material via the photoelectric effect, compton scattering or pair production depending on Z_T and the incident photon energy E_{ph} as will be discussed shortly. Charged particles are able to interact via either rutherford scattering or nuclear interactions depending on m_p . Neutron interaction is facilitated via elastic and inelastic scattering as well as transmutation reactions. In general, all the interaction mechanisms can be classified either as a displacement damage effect or an ionization effect.

2.2.2 Nomenclature

The technical jargon involved in describing radiation effects on microelectronic devices is described in this section.

The total number of particles that have crossed a given area is known as the

fluence and has units of *particles/cm²*. Quite often, post-radiation measurements on irradiated devices are made at specific fluence levels to characterize the damage.

The number of particles crossing a given area per unit time is known as the *flux* and has units of *particles/cm²s*.

In the case of photons, the ionizing radiation dose that is absorbed is the primary metric of interest. The primary unit of radiation damage in semiconductors is the *rad* (radiation absorbed dose). One *rad* is defined as 100 *ergs* per gram of energy absorbed in the exposed crystal (100 *rad* = 1 *Grey* (*Gy*)). Moreover, the *rad* is a material dependant unit, and as such it is typical to specify the material under consideration. In the case of SiGe HBTs *rad(Si)* (1.000*rad*(*SiO₂*) = 0.945*rad*(*Si*)) are most commonly used.

Displacement damage is often quantified via the nonionizing energy loss rate (*NIEL*). *NIEL* has the same units as the linear energy transfer (*LET*) and can also be calculated from first principles based on differential cross sections and reaction kinematics. The theoretical expression for *NIEL* is given in Equation 18.

$$NIEL = \frac{N}{A} \int L[T(\Theta)] T(\Theta) \left\{ \frac{d\sigma}{d\Omega} \right\} d\Omega \quad (18)$$

In the above expression, *NIEL* depends on Avogadro's number, (*A*), target material atomic weight (*A*), differential cross-section in Θ direction ($\frac{d\sigma}{d\Omega}$), the recoil energy (*T*(Θ)) and the percentage of recoil accounted for by displacement (*L*[*T*(Θ))] [3].

2.2.3 The Space Environment

The space environment surrounding the earth and encountered by satellites in orbit, are the primary focus of this section. The sources of particles here are four-fold: (i) protons and electrons residing in the Van Allen belts, (ii) heavy ions trapped in the magnetosphere, (iii) protons and heavy ions from cosmic rays and (iv) protons and heavy ions from solar flares. All of these phenomenon are intimately dependant on the solar cycle [28]. The radiation belts, encountered by

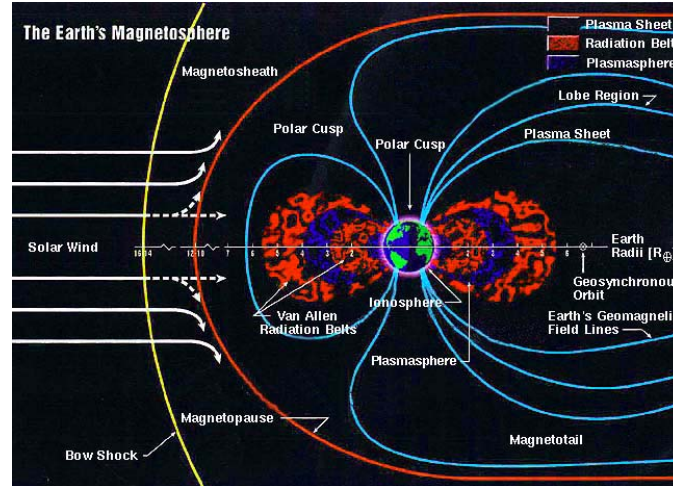


Figure 9: Solar wind and radiation belts encompassing the Earth (after [29]).

satellites in orbit around the earth, are illustrated in Figure 9. The Van Allen belts consist primarily of low energy electrons (a few MeV) and high energy protons (several hundred MeV) in addition to some heavy ion particles trapped in the earth's magnetic field [30]. Galactic cosmic rays incorporate a range of elements with atomic numbers ranging from hydrogen to uranium, typically characterized via low flux levels and a large distribution of particle energies (a few MeV to several hundred GeV) [28]. The fractional composition of particles in these rays has been determined to be 85% protons, 14% alpha particles and 1% heavy ions [31]. In the case of solar flares, high energy protons (hundreds of MeV) are typically involved. Solar flares are typically observed during periods of solar maxima [28].

The exact environment encountered by a satellite in orbit depends on many factors including orbital path or trajectory, solar activity, and mission length. IEEE Standard 1156.4 is used to classify these orbits as low, medium, geostationary and highly elliptical earth orbits [2]. In the case of low energy orbits (LEO), orbital paths take the satellite through the van allen belts several times over a 24 hour period with an altitude of between 200 and 600km. In the case of highly elliptical orbits, the altitude is in the range of 30,000km thereby resulting in longer exposures to cosmic and solar flare environments [28].

The microelectronic devices and circuits exposed to these environments are therefore subject to particles and photons across a wide range of energies and flux. The observed effects on a device and circuit level can be coupled to the fundamental interaction mechanisms between the semiconductor material and the incident radiation. These can be classified as either (i) displacement damage or ionization damage depending on the creation of electron-hole pairs and/or the displacement of atoms from their lattice site. The displacement damage models are discussed for both Si and SiGe in the next section.

2.3 Displacement Damage

Particles incident on a semiconductor lattice structure with sufficient mass are able to displace individual atoms from their lattice sites (depending on energy and trajectory) generating vacancy-interstitial pair defects. This process is known as displacement damage, and can occur for protons, neutrons as well as heavy ions. A vacancy is the absence of an atom from its regular lattice site, whereas an interstitial is an atom located in an off-grid position from the lattice. These defects can then be further classified according to their spatial disposition in the lattice. A vacancy-interstitial pair that is close together is commonly known as a *Freknel – Pair* or a *close – pair*. Two adjacent vacancies are collectively referred to as a *divacancy* and in a similar fashion two adjacent interstitials are referred to as a *di – interstitial*. Very often, the presence of impurities (whether intentional or not) can lead to the formation of defect-impurity complexes such as *vacancy – impurity complexes* and *interstitial – impurity complexes*. Additionally, defects may be either simple (a few atoms displaced together) or defect clusters (longer chains of disordered atoms). In silicon, high-energy neutron irradiation can produce defect clusters, whereas low-energy electron, gamma-ray and proton irradiations can result in simple defects [32]. A typical example of a simple defect, resulting from displacement damage in a crystal lattice is illustrated in Figure 10. For space environments, displacement effects are primarily the result

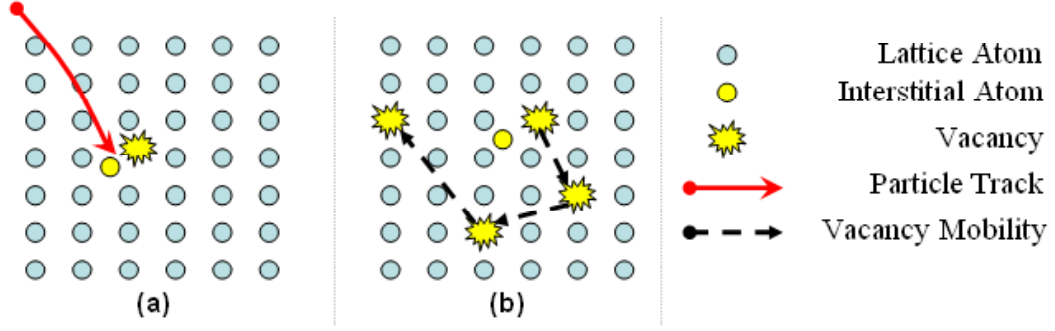


Figure 10: Displacement effects in a crystal lattice (a) energetic particle creates interstitial-vacancy pair (b) vacancy pair migrates throughout lattice.

of high-energy protons and electrons. In military and nuclear reactor applications neutrons are a major concern. The presence of vacancies in the crystal lattice is effectively translated to energy trap states (E_T) in the energy band gap (E_g). Both deep ($E_T \approx E_C - \frac{E_g}{2}$) and shallow ($E_T \approx E_C$, $E_T \approx E_V$) level traps are created. Defects created via displacement can re-order to more stable configurations. In particular, vacancies can be likened to a hole and are mobile in the lattice at room temperature, and as a result will migrate to form more-complex defects such as divacancies and vacancy impurity complexes whose mobility is reduced thereby making them a more stable long-term defect [28]. All defects in the lattice can be detected via device level measurements of optical and electrical properties (a direct result of the E_T levels). Some of these processes are outlined below and are covered in more detail in [33] (and references therein) and are illustrated in Figure 11. Firstly, deep trap levels result in the thermal (Shockley Read Hall) generation (and recombination) of electron-hole pairs. For generation, a bound-state valence electron is promoted from E_V to E_T and then from E_T to E_C . In the case of carrier recombination, the exact opposite process occurs when an electron (in E_C) and a hole (in E_V) both come spatially close to the defect site and are both annihilated at the trap energy, E_T . In this case, E_T must be close to the midgap level to have any appreciable effect [34].

Shallow level traps result in the temporary trapping of carriers at the trap

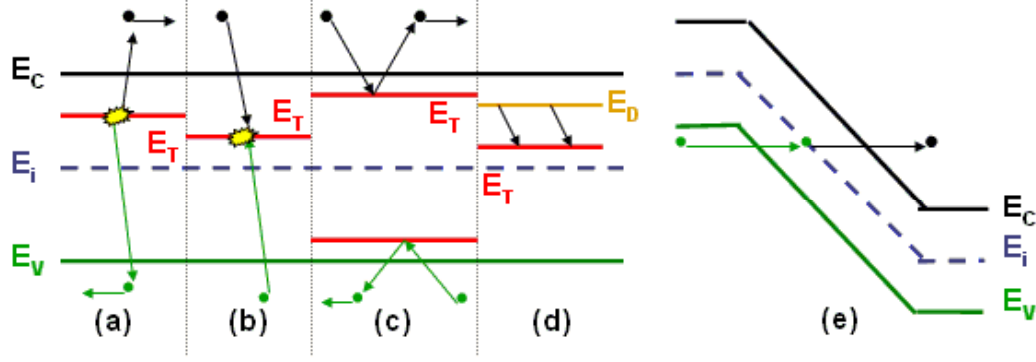


Figure 11: Defects create trap levels in the bandgap that interfere with the dynamics of charge transport via (a)generation, (b)recombination, (c)trapping, (d)compensation and (e)tunneling (after [35])

energy, E_T . The carriers are usually later returned to their band with no long term recombination taking place.

Trap centers (both deep and shallow) may also result in the compensation of dopants or impurities in the lattice. This results in a reduction in the equilibrium majority carrier concentration, which results in an increase in the collector resistance R_C for bipolar transistors.

Defect levels (especially deep levels) can also enable the tunneling of carriers through potential barriers. This is accomplished through an effective reduction in the barrier height, and width (when under bias). This can cause an increase in the tunneling component of reverse-bias currents in pn-junction diodes.

Radiation induced trap centers can serve as scattering centers and result in a subsequent reduction in carrier mobilities. These effects are amplified at lower temperatures, and higher doping levels where ionized impurity scattering (which can be likened to radiation induced trap centers) dominates over traditional lattice scattering [7].

Depending on the energy level of the trap formed, carrier density, impurity concentration and temperature any one of the mechanisms described above may dominate, or they may all act in concert. For simple defects (single interstitials or vacancies) mobility and activation energy is dependant on the charge state of

Table 4: Electrical characterization of the dominant radiation defects in Si at 300K (after [28]).

Defect Center	$E_T(\text{eV})$	$c_n(\text{cm}^3/\text{s})$	$c_p(\text{cm}^3/\text{s})$	$T(\text{K})$
$V - O^{0/-}$	0.164	$1.4 \times 10^{-8} x T^{0.5}$	$8 \times 10^{-8} x T^{0.7}$	80 - 108
$V - V^{-/--}$	0.225	$1.6 \times 10^{-12} x T^{1.4}$	7×10^{-7}	105 - 155
$V - V^{0/-}$	0.421	$5.4 \times 10^{-9} x T^{0.4}$	$2 \times 10^{-6} x T^{-0.3}$	182 - 266
$V - V^{+/0}$	0.194	$>> c_p$	$2.1 \times 10^{-9} x T^{0.2}$	104 - 146
$C_i O_i$	0.339	$5.1 \times 10^{-23} x T^{5.2}$	$1.2 \times 10^{-10} x T^{0.61}$	160 - 238

the defect. The charge state of a defect is indicative of the number of electrons associated with that defect and is determined by $E_F - E_T$ [35].

2.3.1 Silicon

In this section a literature review of defects in Si is presented. The electrical impact of these defects is a function of the defect trap density N_T , energy trap level E_T , and the electron and hole capture cross sections σ_n and σ_p respectively. Deep Level Transient Spectroscopy (DLTS) is an analytic technique used to characterize energy trap states via a capacitance transient measurement achieved through applying a pulsed bias to the sample over a wide temperature range [36]. DLTS has been successfully employed to identify the dominant radiation defect traps in Si that are stable at 300K [37]. The results are illustrated in Table 4 [28]. c_n and c_p are the electron and hole capture rates respectively. Experimental studies on both p- and n-type proton irradiated Si have identified the $E_T = 0.421\text{eV}$ and $E_T = 0.164\text{eV}$ as the dominant recombination centers for the low- and high-injection regimes of operation based on calculations of the respective recombination lifetimes [37, 38, 39]. To be sure, there are several challenges associated with the accurate identification of radiation induced deep level traps in Si including the background dopant density and the presence of longer cluster type defects that tend to broaden vacancy peaks [28].

Additionally, Electron Paramagnetic Resonance (EPR) and Localized Vibrational Mode (LVM) spectroscopy have been successfully employed to characterize the

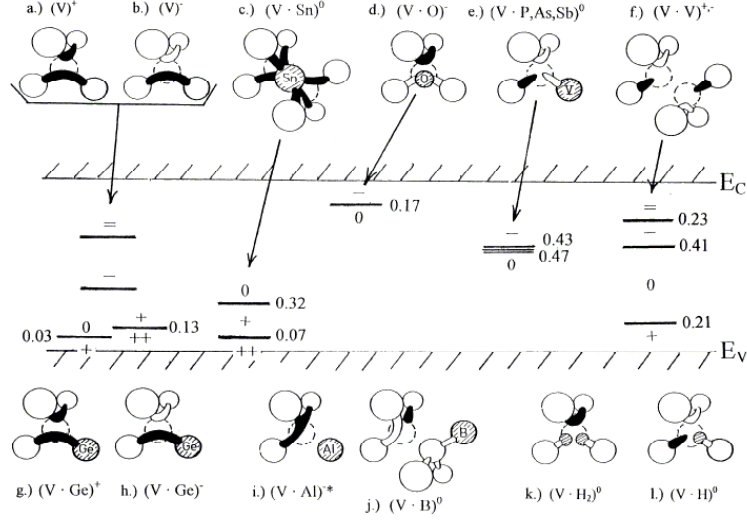


Figure 12: Energy level and structure of intrinsic Si vacancies (after[40]).

energy levels and structures of intrinsic defects in Si [40]. These results are displayed in Figure 12.

2.3.2 Silicon-Germanium Alloys

Radiation induced defects in SiGe alloys have been studied for both bulk films [41, 42], as well as strained and relaxed epitaxial layers [43, 44]. Epitaxially grown SiGe alloys are however, far more important than their bulk counterparts as they form the key component of many state of the art devices. The material in this section is therefore devoted to radiation effects in epitaxial SiGe alloys.

Low energy proton exposures (2MeV and $1.5 \times 10^{12} p/cm^{-2}$) on relaxed n-type $Si_{1-x}Ge_x$ performed on high quality films have allowed for the identification of prominent radiation induced defects [43]. The findings from these studies indicate that the concentration of defects is inversely proportional to the Ge fraction, x . Additionally, it was concluded that while the same basic traps are present, their corresponding trap levels are dependant on x [43]. Work on proton irradiated relaxed p-type $Si_{1-x}Ge_x$ yield a similar compositional dependency for the observed defect levels with additional hole traps at the mid gap energy level ($E_G/2$) being identified via DLTS for ($x > 0.05$) [44]. High temperature annealing of

Table 5: Electrical characterization of the dominant radiation defects in relaxed $Si_{1-x}Ge_x$ epilayers (after [28]).

Ge-Fraction	Defect Type	$E_a(eV)$	$\sigma_\infty(cm^2)$	$T_A(K)$
5 (n-Sb)	$E_C - 0.101$	9×10^{-16}	-	C_i
5 (n-Sb)	$E_C - 0.158$	2.8×10^{-16}	-	$OV (A\text{-center})$
5 (n-Sb)	$E_C - 0.264$	5×10^{-15}	-	$V/V^{-/--}$
5 (n-Sb)	$E_C - 0.290$	5×10^{-16}	-	$Ge/V^{-/--}$
5 (n-Sb)	$E_C - 0.434$	1.9×10^{-15}	295-315	$SbV + VV^{0/-}$
30 (n-P)	$E_C - 0.32$	10^{-15}	560	$V/V^{-/--}$
30 (n-P)	$E_C - 0.49$	2×10^{-15}	470	PV
25 (n-Sb)	$E_C - 0.51$	$6 - 8 \times 10^{-16}$	-	SbV
15 (p-B)	$E_V + 0.14_a$	4×10^{-16b}	550	$VV^{+/0}$
25 (p-B)	$E_V + 0.13_a$	5×10^{-15b}	650-700	B_iC_S

the post- radiation film has also been observed to modify the trap characteristics. Additionally, the stability of hole traps is observed to increase with increasing x . This is a similar trend to that observed for vacancy defects that become more stable via association with Ge impurities in a bulk Si film. The main radiation induced defects in relaxed $Si_{1-x}Ge_x$ film are illustrated in Table 5 [28]. Strained $Si_{1-x}Ge_x$ films are very attractive as a template for mobility enhancement in Si based devices [45, 46]. 5.4MeV α particle irradiations have been performed on n-type strained $Si_{0.6}Ge_{0.4}$ epitaxial films [47]. In agreement with the results obtained for relaxed $Si_{1-x}Ge_x$ films, a reduction in the trap concentration with increasing x has been observed for identical particle fluence. p-type $Si_{1-x}Ge_x$ strained layer epitaxial films make up the base region of advanced npn SiGe HBTs and as such their response to a myriad of particle irradiations has been extensively studied [48, 49, 51, 5, 52]. The results from these studies bring to the fore several interesting conclusions regarding the radiation effects on strained layer $Si_{1-x}Ge_x$ epitaxy. It has been repeatedly shown that dopant de-activation, trap concentration, and trap levels are functionally inversely proportional to the Ge fraction, x . One possible explanation of this phenomenon is the reduction in the creation of primary knock on atoms (PKA's) for increased x [28].

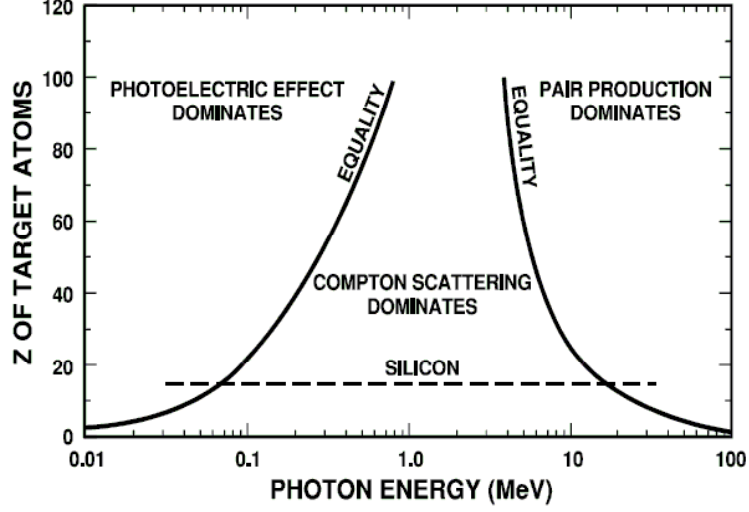


Figure 13: Competing mechanisms in photon interactions with matter (after [53]).

2.4 Ionization Damage Mechanisms

Ionization damage in lattice structures results from the creation of a "charged funnel track" along the path of the incident particles. The passage of ionizing radiation through matter can be effectively studied by considering both (i) electromagnetic radiation with photons from γ and x-rays and (ii) heavy and light charged particles such as protons and electrons.

2.4.1 Photon Interaction With Matter

The three primary means of interaction of photons with matter are (i) the photoelectric effect, (ii) Compton scattering and (iii) pair production. The interaction mechanism that dominates is a function of the photon energy (E_{ph}) and the atomic number of target atoms (Z_T) as illustrated in Figure 13.

2.4.1.1 The Photoelectric Effect

In the regime of photon energies ($E_{ph} < 0.5 \text{ MeV}$) the entire quanta of photon energy may be absorbed by electrons in the innermost atomic shells (such as the K-shell). If E_{ph} is larger than the binding energy of the electron B_e it results in

the release of an electron from the atom (ionization) with kinetic energy given by Equation 19.

$$T = E_{ph} - B_e \quad (19)$$

In addition, the residual atom gains recoil energy in order to satisfy the conservation of momentum and energy. The ionization of the atom depends both on the atomic number of the target Z_T and the binding energy of the electron B_e (shell dependent). Approximate binding energies are listed in Equations 20, 21 and 22 [27].

$$(B_e)_K = Ry(Z - 1)^2 \quad (K - \text{shell binding}) \quad (20)$$

$$(B_e)_L = \frac{1}{4}Ry(Z - 5)^2 \quad (L - \text{shell binding}) \quad (21)$$

$$(B_e)_M = \frac{1}{9}Ry(Z - 13)^2 \quad (M - \text{shell binding}) \quad (22)$$

The Rydberg constant (Ry) is defined in Equation 23.

$$Ry = hcR = hc \frac{2\pi^2 m_e e^4}{ch^3} = \frac{m_e e^4}{2\hbar^2} \equiv 13.61 \text{ eV} \quad (23)$$

In the above expression $R = 1.097 \times 10^5 \text{ cm}^{-1}$ is the spectroscopic Rydberg constant for infinite mass. Additionally, the total binding energy of the atom can be expressed as shown in Equation 24.

$$(B_e)_{tot} = 15.73 Z^{7/3} \text{ eV} \quad (24)$$

At lower values of E_{ph} , photoelectrons are emitted in a direction that is perpendicular to the incident photons. As E_{ph} is increased the emitted photoelectron distribution peaks more to a forwardly directed emission.

2.4.1.2 Compton Scattering

In compton scattering, the incident photon (with energy E_{ph}) impacts a nearly free electron (assumed to be at rest). The electron recoils with kinetic energy, T , and the photon is scattered in a different direction with energy E'_{ph} . The energy

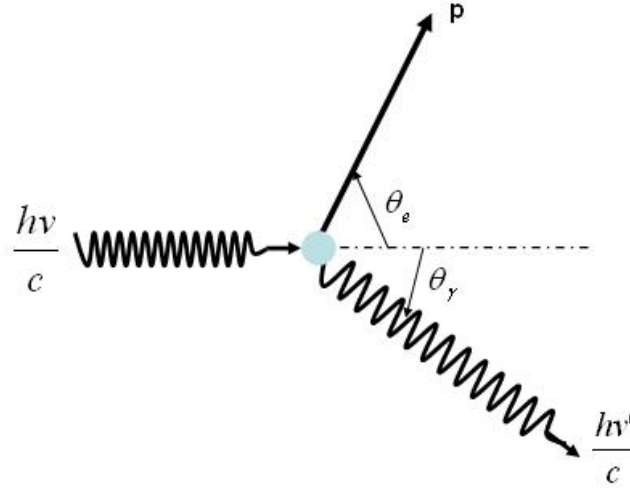


Figure 14: Compton scattering of an incident photon by a quasi free electron (after [27].)

transfer in this process is governed by the conservation of energy and is given in Equation 25.

$$T = E_{ph} - E_{ph}' = E - mc^2 \quad (25)$$

The decrease in the photon energy to E_{ph}' effectively translates into an increase in wavelength as depicted in Figure 14. Conservation of momentum in the directions parallel and perpendicular to the incident photon generates Equation 26 and 27.

$$\frac{h\nu}{c} = \frac{h\nu'}{c} \cos \theta_y + p \cos \theta_e \quad (26)$$

$$0 = \frac{h\nu'}{c} \sin \theta_y + p \sin \theta_e \quad (27)$$

The difference between the wavelength of the incident photons and scattered photons is known as the Compton shift and is given in Equation 28.

$$\Delta\lambda \equiv \lambda' - \lambda \equiv \frac{c}{\nu'} - \frac{c}{\nu} = \lambda_C(1 - \cos \theta_y) \quad (28)$$

The maximum shift in wavelength, and hence the maximum energy transfer occurs for $\theta_{ph} = 180^\circ$ and is given as $\Delta\lambda_{max} = 2\lambda_C$, where λ_C is the Compton wavelength.

The scattered photon energy ($E_{ph(out)}$) can be expressed in terms of the scattering angle via Equation 29. A scattering angle of $\theta_{ph} = 180^\circ$ corresponds to the

maximum $E_{ph(out)}$ and minimal compton shift $\Delta\lambda_{max} = 0$.

$$\frac{E_{ph(out)}}{E_{ph(in)}} = \frac{h\nu'}{h\nu} = \frac{1}{1 + \varepsilon(1 - \cos \theta_{ph})} \quad (29)$$

The reduced incident photon energy is given as $\varepsilon \equiv \frac{h\nu}{m_e c^2}$. Additionally, the kinetic energy of the scattered photon T can be expressed in terms of the scattering angles θ_{ph} and θ_e as shown in Equation 30 and Equation 31.

$$T = h\nu \frac{\varepsilon(1 - \cos \theta_{ph})}{1 + \varepsilon(1 - \cos \theta_{ph})} \quad (30)$$

$$T = h\nu \frac{2\varepsilon \cos^2 \theta_e}{(1 + \varepsilon)^2 - \varepsilon^2 \cos^2 \theta_e} \quad (31)$$

Then for $\theta_{ph} = 180^\circ$ and $\theta_e = 0^\circ$ the recoiled electron has its maximum kinetic energy T_{max} given from Equation 32.

$$T_{max} = \frac{h\nu}{1 + \frac{1}{2\varepsilon}} \quad (32)$$

The scattering angles θ_{ph} and θ_e are related by the expression in Equation 33.

$$\cot \theta_e = (1 + \varepsilon) \tan \frac{\theta_{ph}}{2} \quad (33)$$

2.4.1.3 Electron-Positron Pair Production

As the photon energy is increased further $2m_e c^2 > 1.02 \text{ MeV}$ it is possible to create electron-positron pairs. The excess energy over $2m_e c^2$ is manifested as kinetic energy for both particles with energies related by Equation 34.

$$T_- + T_+ = E_{ph} - 2mc^2 \quad (34)$$

In this case the E_{ph} is significantly larger than the sum of the kinetic energies (T_+ and T_-). The excess energy here is accounted for in the rest masses of the electron and positron. In particular, the positron can be considered to be an "anti-electron" and upon slowing down it will annihilate with an electron releasing more γ rays which will in turn interact with the material via either compton scattering or the photoelectric effect [54].

2.4.2 Charged Particle Interaction with Matter

The interaction of charged particles with matter can produce both ionization and displacement effects as previously mentioned. The effects are realized primarily through either rutherford scattering, or nuclear interactions.

2.4.2.1 Rutherford Scattering

In 1911, Rutherford was able to derive the correct expressions for the classical differential cross-section of a charged particle under the influence of a Coulombic force leading to the discovery of the nucleus [55]. Rutherford's work was the result of analysis on experimental results from Geiger and Marsden [56, 57] that showed surprisingly high levels of back-scattered α particles being repelled from a gold foil target. These results contradicted the then widely accepted Thomson "plum pudding" model that regarded the α particle as a uniformly distributed cloud of positive charge.

In the new model, an incident particle with charge Z_i , mass m_i is assumed to approach a target atom of charge Z_T , mass M_T where $M_T \gg m_i$. The coulombic interaction between the two particles results in a hyperbolic path of approach for the incident particle as illustrated in Figure 15 [27]. The incident particle is presumed to have an initial velocity \vec{u} . The principle of energy conservation yields the collision diameter b shown in Equation 35, and the impact parameter D shown in Equation 36 can be determined.

$$b = \frac{Z_i Z_T}{\frac{1}{2} m_i u^2} \quad (35)$$

$$D^2 = x^2 \frac{v^2}{u^2} = x(x - b) \quad (36)$$

The scattering angle is defined as $\vartheta = \pi - 2\alpha$. The corresponding differential cross section for this interaction is given in Equation 37.

$$\sigma_R(\vartheta') \equiv \sigma_C(\vartheta) \equiv \frac{d\sigma'}{d\Omega'} \equiv \frac{b^2}{16 \sin^2\left(\frac{\vartheta'}{2}\right)} \equiv \left(\frac{Z_i Z_T}{\frac{1}{2} \mu u^2} \frac{1}{4 \sin^2\left(\frac{\vartheta'}{2}\right)} \right)^2 \quad (37)$$

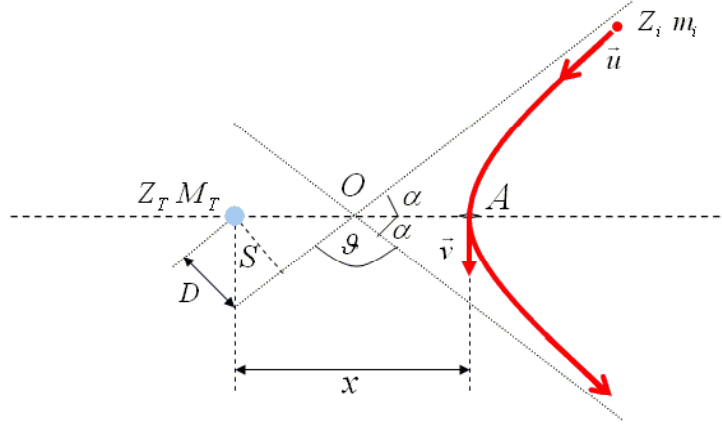


Figure 15: Rutherford scattering resulting from the coulombic interaction between an incident particle m_i and target particle M_T (after [27].)

Where μ is the reduced mass given by $\mu = \frac{m_i M_T}{m_i + M_T}$. The functional form relating the differential cross section σ_R to the scattering angle θ' is of the form $\frac{1}{\sin^4(\frac{\theta'}{2})}$. This results in a maximized cross section for interaction for low scattering angles.

2.4.2.2 Heavy Particle Interactions

While rutherford scattering applies primarily to charged particles that undergo elastic scattering, there are several other mechanisms for charged particles to interact with matter. These include (i) elastic collisions with bound electrons, (ii) inelastic collisions with bound electrons (iii) elastic collisions with nuclei and (iii) inelastic collisions with nuclei [27]. Typically particles with low energies (hundreds of eV) and low masses (such as electrons) are more likely to undergo elastic collisions (i) and (iii). Inelastic collisions with bound electrons are more probable for heavy particles such as mesons, protons, deuterons and α particles.

The energy deposited by an energetic particle in the lattice is often characterized by the linear energy transfer (LET) parameter which is simply the energy deposited per unit length in the material ($LET = \frac{dE}{dx}$) in units of $\frac{MeV-cm^2}{mg}$. LET is also referred to as the stopping power and can be expressed quantum mechanically

in the *Bethe – Bloch* formula given in Equation 38 [27].

$$-\frac{dE}{dx} = \frac{4\pi k_0^2 z^2 e^4 n}{mc^2 \beta^2} \left[\ln \frac{2mc^2 \beta^2}{I(1 - \beta^2)} - \beta^2 \right] \quad (38)$$

The above expression is specifically for the stopping power for a heavy charged particle in a uniform medium (such as protons in a crystal lattice). The *LET* depends therefore on the atomic number of the heavy charged particle (z), speed of the particle relative to c (β) and excitation energy of the medium (I).

$$rad = LET \left[\frac{MeVcm^2}{mg} \right] \times fluence \left[\frac{1}{cm^2} \right] \times 1.60 \times 10^{-5} \left[\frac{mg rad}{MeV} \right] \quad (39)$$

The *LET* and particle fluence are then used to calculate the *rad* for heavy ions and protons as shown in Equation 39 [2].

2.5 Radiation Effects in Bipolar Devices

A discussion of the radiation effects in Si-based bipolar technologies is now presented. Three primary damage mechanisms have been identified in the literature [28]. These include increases in the surface recombination velocity s_r , positive oxide trapped charge and bulk damage.

The interface traps (D_{it}) generate a surface recombination in the base-emitter and collector-base depletion regions according to Equation 40 [65]. v_{th} is the thermal velocity, kT the thermal energy, σ_n, σ_p the electron and hole capture cross sections.

$$s_r = 0.5 v_{th} \sqrt{\sigma_n \sigma_p} \pi k T D_{it} \quad (40)$$

s_r demonstrates a slight dependence on particle energy and bias during irradiation. Increases in s_r are manifested in a reduction in transistor gain.

Positive oxide trapped charge is one of the fundamental damage mechanisms in any device that incorporates *Si/SiO₂* interfaces. A schematic representation of the radiation effects in the oxides of MOS devices are illustrated in Figure 16. Electron hole pairs are generated by ionizing radiation and holes are able to transport through localized states in the bulk *SiO₂*. Additionally, there is deep

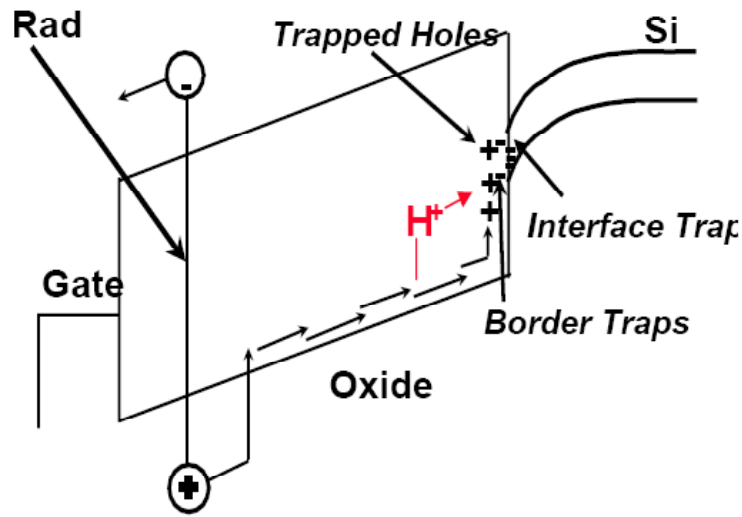


Figure 16: Creation of oxide and interface trap charge in MOS devices (after [58]).

hole trapping at the Si/SiO_2 interface and traps in the bandgap as discussed in previous sections. The effects of this positive oxide trapped charge include carrier inversion, gain reduction, increased leakage and decreased breakdown all demonstrating a strong dependence on the bias during irradiation [28].

Bulk damage is a third mechanism which is primarily realized via displacement damage as discussed previously. Bulk damage is strongly dependent on particle energy and is manifested via gain degradation in the device.

2.6 Summary

In this chapter an overview of the radiation effects on semiconductor materials was presented. Following the introduction, a description of the various radiation environments of interest was discussed. Particular attention was placed on the space environments encountered by satellites in orbit. This was followed by a description of displacement damage effects in Si and SiGe material systems. Finally, a discussion of ionization effects was presented including photon and heavy charged particle interaction with matter and effects of radiation on silicon bipolar technologies.

CHAPTER III

PROTON TOLERANCE OF SIGE HBTS

3.1 Introduction

This chapter presents a comprehensive analysis of the effects of technology scaling on the proton response of state-of-the art fourth-generation SiGe HBTs manufactured at IBM Microelectronics. The details of the experiment design including the devices under test, test facilities and methodology, *dc* and *ac* results on the observed response are explored. The results demonstrate that SiGe HBTs exhibit impressive total dose tolerance, even at unprecedented levels of vertical profile scaling and frequency response. Negligible total dose degradation in β (0.3%), f_T and f_{max} (6%) is observed in the circuit bias regime, suggesting that SiGe BiCMOS technology is potentially a formidable contender for high-performance space-borne applications. Additionally, significant differences in the responses of high- and low-breakdown transistors are explored. The observed results are explained in terms of the variation in the collector doping and the resultant differences in the electric fields present at the CB junction.

3.2 Experiment Design

3.2.1 Test Facilities

Medium energy (63MeV) proton irradiations were performed at the Crocker Nuclear Laboratory at the University of California at Davis. The dosimetry measurements were performed using a five-foil secondary emission monitor calibrated against a Faraday cup. The radiation source (Ta scattering foils) located several meters upstream of the target established a beam spatial uniformity of about 15% over a 2.0 cm radius circular area. Beam currents from about 20 nA to 100 nA allowed testing with proton fluxes from 1×10^9 to 1×10^{12} proton/cm²sec. This dosimetry

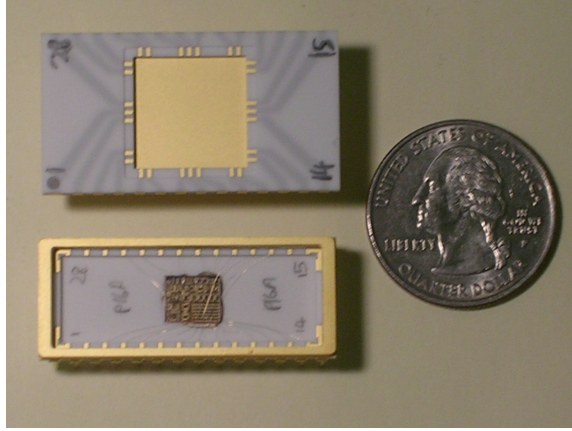


Figure 17: 28-pin dip packages used to facilitate in-situ measurement of irradiated samples.

system has been previously described [59, 60], and is accurate to about 10%. At proton fluences of 1×10^{12} p/cm² and 5×10^{13} p/cm², the measured equivalent total ionizing dose was approximately 135 and 6,759 krad(Si), respectively.

3.2.2 Devices Under Test

The devices selected for test will facilitate the comprehensive comparison of the proton tolerance of the 1st through 4th technology generations. The, 4th-generation 350 GHz SiGe HBT (IBM 9T) investigated featured *dc* test structures of emitter area (A_E) of $0.12 \times 2.5 \mu\text{m}^2$, and was compared to 0.50 μm 50 GHz (IBM 5HP), 0.20 μm 120 GHz (IBM 7HP), and 0.12 μm 200 GHz (IBM 8HP) technology nodes measured under identical conditions in order to facilitate unambiguous comparisons. In the case of the 4th-generation technology, transistors of varying breakdown voltage were used to evaluate the impact of the collector doping profile on the measured proton response. All *dc* test structures packaged in 28-pin dual in-line ceramic packages with the emitter, base and collector terminals wire bonded out to external leads as illustrated in Figure 17. This facilitated easy in-situ measurements at the incremental proton fluences outlined in the previous section and allows for various bias configurations during irradiation. A bias configuration with all terminals grounded was chosen for these irradiations.

Corresponding *ac* test structures, were irradiated at 7.0×10^{12} p/cm² and 5.0×10^{13} p/cm². Wirebonding of *ac* test structures is not compatible with robust broadband measurements without careful calibration of losses due to bond-wire inductance. *ac* test structures are therefore irradiated passively (with all terminals floating). Previous investigations have demonstrated that irradiations conducted with all terminals grounded exhibited similar degradation to the case with all terminals floating for 1st generation devices [61]. Additional work performed on different biasing schemes (forward active, reverse active) reveals that strong electric fields present in the device can further degrade the post-radiation device performance [62]. On-wafer probing of S-parameters is therefore used to characterize the high-frequency device performance. The post-irradiated samples were characterized at room temperature with an Agilent 4155 Semiconductor Parameter Analyzer (*dc*) and an Agilent 8510C Vector Network Analyzer (*ac*) using the deembedding techniques discussed in [63].

3.3 *dc Results*

The post-irradiation forward-mode Gummel characteristics on a low breakdown-voltage transistor (High N_C) are shown in Figure 18 and clearly depict the characteristic monotonic increase in the base current density ($J_B = I_B/A_E$) as a function of proton fluence. This classical signature of radiation-induced damage in SiGe HBTs is attributed to radiation-induced G/R trap centers, physically located near the EB spacer oxide where they are able to perturb the dynamics of charge transport at the EB junction [64]. Measurements performed at room temperature, approximately six weeks after the exposure yielded a slight decrease in J_B , indicative of an underlying "self-annealing" mechanism. This is essentially the result of a defect-reordering process occurring within hours of the initial radiation burst, referred to as *transient* or *rapid* annealing in the literature [33]. The damage measured here, six weeks after the initial irradiation, is termed permanent damage. Literature has also shown that a long-term anneal has also been observed

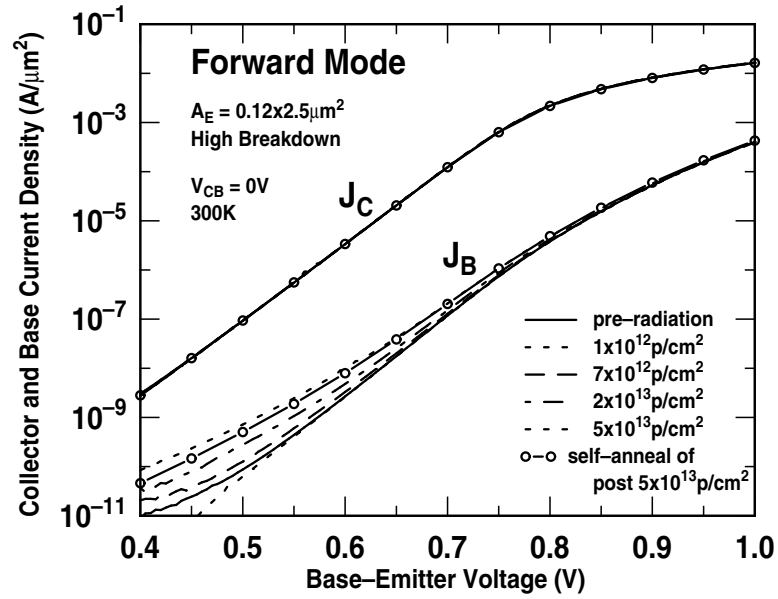


Figure 18: 4th-generation post-radiation Forward-mode Gummel characteristics showing an increasing G/R J_B and self-annealing after 6 weeks.

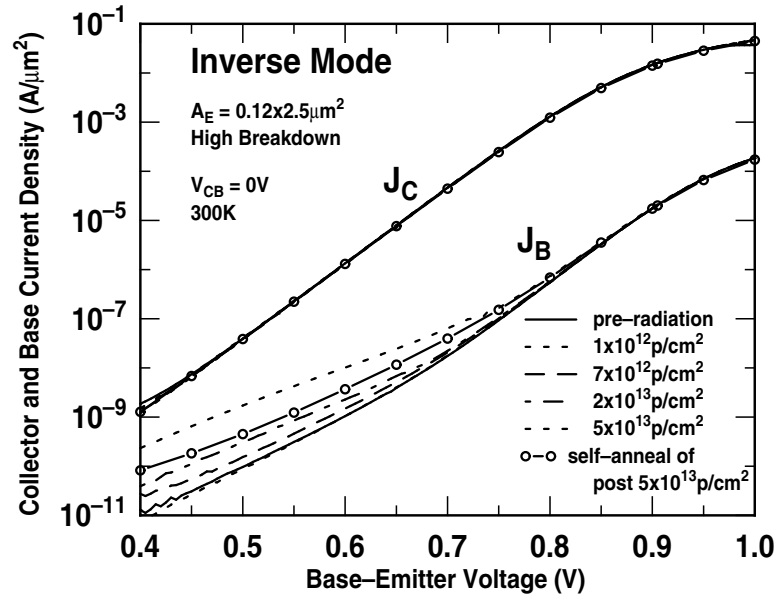


Figure 19: 4th-generation post-radiation Inverse-mode Gummel characteristics showing an increasing G/R J_B and self-annealing after 6 weeks.

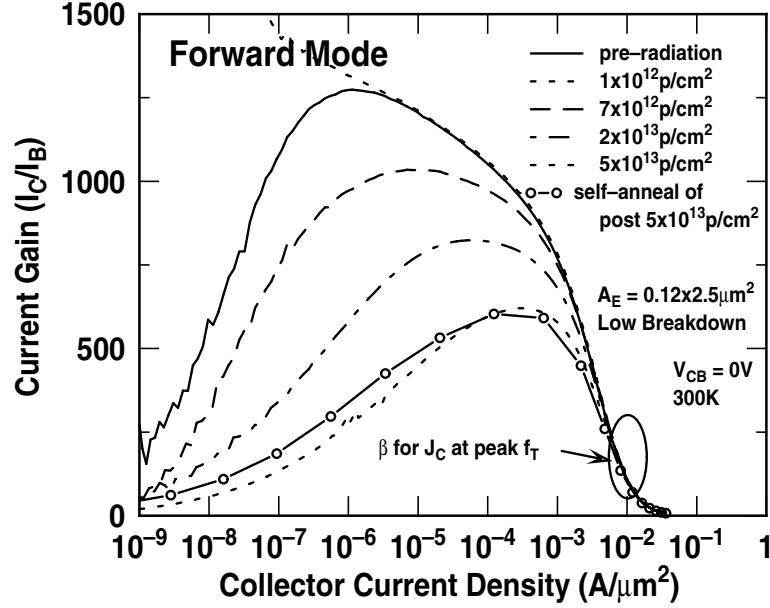


Figure 20: 4th-generation post-radiation β characteristics showing a reduction in β_{peak} , but no change in β at peak f_T with proton fluence.

resulting in improvements in key device metrics by factors as large as two, for neutron damage [33].

Similar results obtained for the inverse-mode Gummel characteristics (emitter and collector terminals swapped) are illustrated in Figure 19. The inverse-mode gummel degradation is representative of radiation-induced G/R trap centers, this time located near the shallow trench edges (STI) [64]. In this case, charge transport dynamics at the CB junction is affected.

The forward-mode dc current gain ($\beta = I_C/I_B$) is depicted in Figure 20. A degradation in β_{peak} with increasing proton fluence is observed, as would be expected from the gummel characteristics. This 40% decrease in β_{peak} is accompanied by a shift in the occurrence of β_{peak} to higher values of J_C . This is expected since the excess base current, generated by the G/R traps, is only dominant in the low injection regime of device operation as the dynamics of carrier interaction with the trap level is functionally dependant on the carrier density itself [4]. More importantly, however, there is practically no change (less than 0.3% decrease) in β at peak f_T . This observation is quite significant since in order to extract maximal

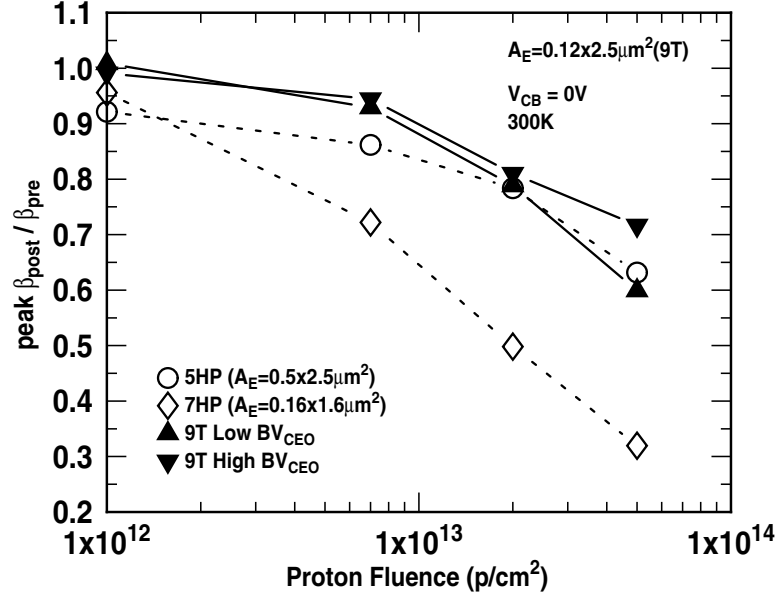


Figure 21: β_{peak} degradation as a function of proton fluence for 1st-, 2nd-, 3rd- and 4th-generation (high and low N_C) devices.

switching speed from these devices for circuit applications, the transistors are often biased at a J_C that is close to the peak f_T of the technology. These results bode well for circuit designers as it implies that β mismatches in transistor performance resulting from incident radiation is negligible.

Three *dc* Figures-of-merit were used to compare the proton tolerance across multiple SiGe HBT technology generations. These are the β_{peak} degradation ($\beta_{peak,pre}/\beta_{peak,post}$), forward- and inverse-mode I_B degradation ($\left. \frac{I_{B,post}}{I_{B,pre}} \right|_{V_{BE}=0.6V}$). These metrics are plotted in Figures 21, 22 and 23. The increased radiation-induced I_B degradation in 2nd-generation SiGe HBTs compared to that found in the 1st- has previously been attributed to a stronger electric field in the EB junction at the device periphery, which is a direct consequence of both the higher local doping and vertical and lateral scaling [52]. The increased β_{peak} degradation for 2nd-generation devices supporting this claim is evident in Figure 21. These observations suggest that changes in the device cross section can have an impact in the observed radiation tolerance of the transistor. An analysis of β_{peak} degradation, shown in Figure 21, reveals that the 4th- generation devices, exhibit a degradation

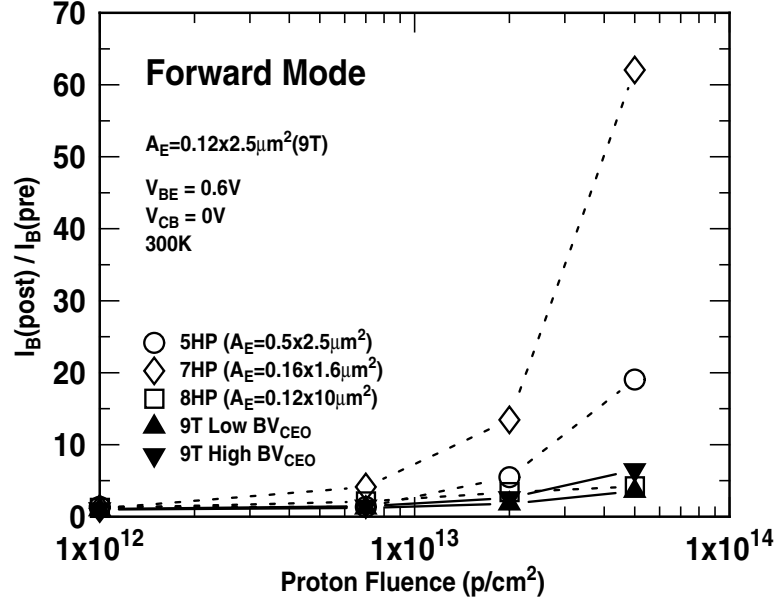


Figure 22: Forward-mode I_B degradation for 1st-, 2nd-, 3rd- and 4th-generation (high and low N_C) devices.

similar to that of the 1st-generation device, while achieving superior performance metrics. Again here, changes in the structure, this time to the "raised extrinsic base structure" result in a change in the proton tolerance of the device. The forward- and inverse-mode post-radiation I_B degradation are depicted in Figures 22 and 23 respectively. There are substantial improvements in both the forward- and inverse-mode post-radiation I_B degradation respectively for both the 3rd-, and 4th-generation SiGe HBTs when compared to their prior technology nodes. As expected, there was no significant difference between the forward-mode I_B degradation for high and low breakdown transistors, in the inverse-mode I_B degradation however, the low-breakdown device, with its higher N_C and increased CB electric fields displayed a notably increased base current leakage.

The observed improved radiation tolerance for both the 3rd-, and 4th-generation devices can easily be explained by the "raised extrinsic base" configuration that results in EB and CB junctions that are physically further removed from the STI edges. The result is that the radiation induced oxide trapped charge is now further removed from the junctions leading to a reduction in the observed damage [65].

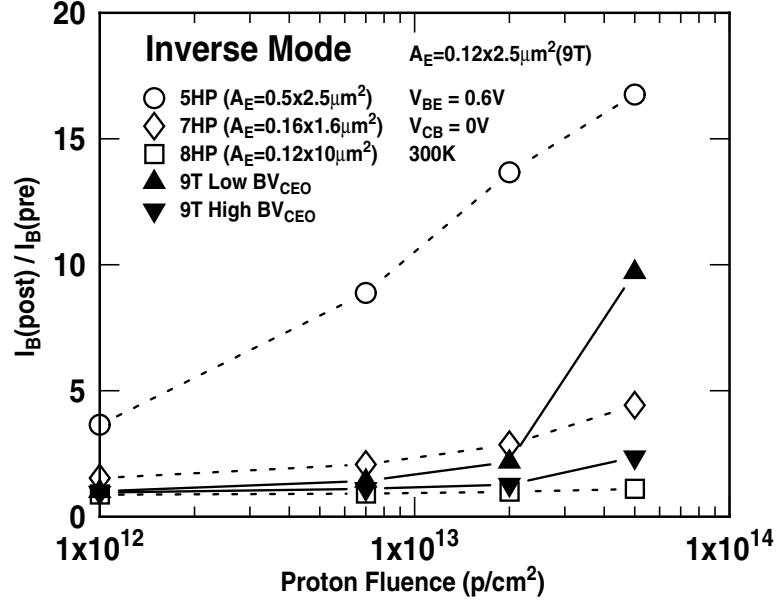


Figure 23: Inverse-mode I_B degradation for 1st-, 2nd-, 3rd- and 4th-generation (high and low N_C) devices.

Additionally, the effective trap density D_{it} , near both junctions is such that there is less carrier recombination and hence ΔI_B is reduced. It should be emphasized that these improvements are achieved solely through the migration to the new raised extrinsic base structure and is not the result of any intentional radiation-hardening processes.

3.4 ac Results

The transistor scattering parameters (S-parameters) for the low-breakdown, high-performance device ($f_T = 350\text{GHz}$), were characterized to 45 GHz over a range of bias currents, each at a constant collector-base voltage V_{CB} . This data was then subsequently de-embedded using standard "open-short" structures to calculate the small-signal current gain ($h_{21} = \frac{i_c}{i_b} \Big|_{v_c=0}$) and the Mason's unilateral gain ($U = \frac{|Y_{21} - Y_{12}|^2}{4(G_{11}G_{22} - G_{12}G_{21})}$) described in [66].

f_T data points were then obtained using a -20dB/decade slope extrapolation of h_{21} for different proton fluences, as shown in Figure 24 for both pre-radiation and a post-radiation fluence of $5 \times 10^{13} \text{ p/cm}^2$. f_T is defined as frequency at

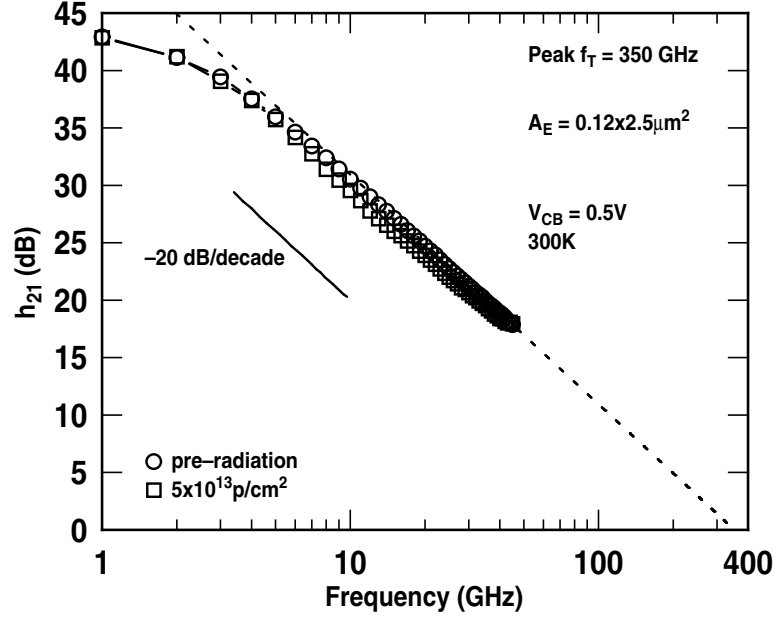


Figure 24: h_{21} extrapolation used to determine f_T for 4th-generation SiGe HBTs.

which the short circuit current gain of the transistor h_{21} , becomes unity. f_{max} is determined as the frequency at which the maximum operating power gain $G_{p,max}$, becomes unity. As evidenced in the Figure, both pre- and post-radiation h_{21} data are remarkably robust. An overlay of pre- and post-radiation measurements of f_T vs J_C for 1st-, 2nd-, 3rd- and 4th-generation SiGe HBTs, shown in Figure 26 verify that their *ac* performance continues to be remarkably tolerant to incident proton irradiation, even for novel device structures employing both aggressive vertical scaling and reduced thermal cycle processing. Specifically, in the case of the 4th-generation SiGe HBT there is a moderate 6% decrease in both f_T and f_{max} as depicted in Figure 26.

The dynamic base resistance (r_{bb}), was extracted from measured S-parameters and is shown in Figure 27. A slight increase in r_{bb} at 5×10^{13} p/cm², for J_C close to peak f_T is observed and is consistent with the moderate 6% decrease in the peak f_{max} , previously attributed to displacement effects in the neutral base region and the deactivation of boron dopants [5]. For lower J_C values, pre- and post-radiation r_{bb} are both exhibit significant fluctuation. This can be attributed

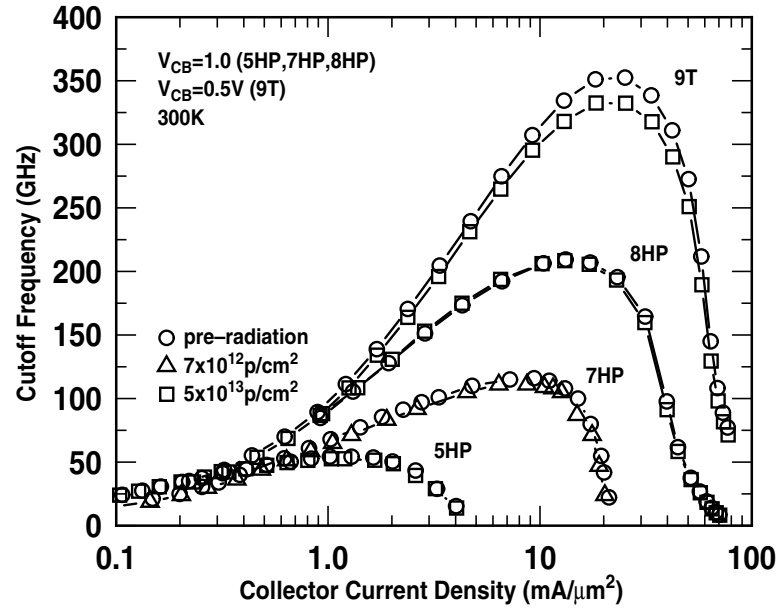


Figure 25: Pre- and post-radiation f_T for 1st-, 2nd-, 3rd- and 4th-generation SiGe HBTs.

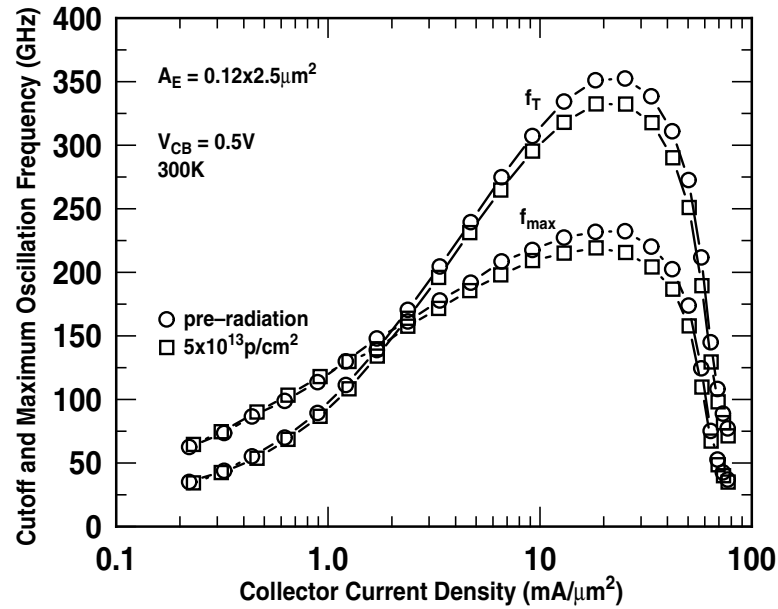


Figure 26: Pre- and post-radiation f_T and f_{max} for 4th-generation SiGe HBTs.

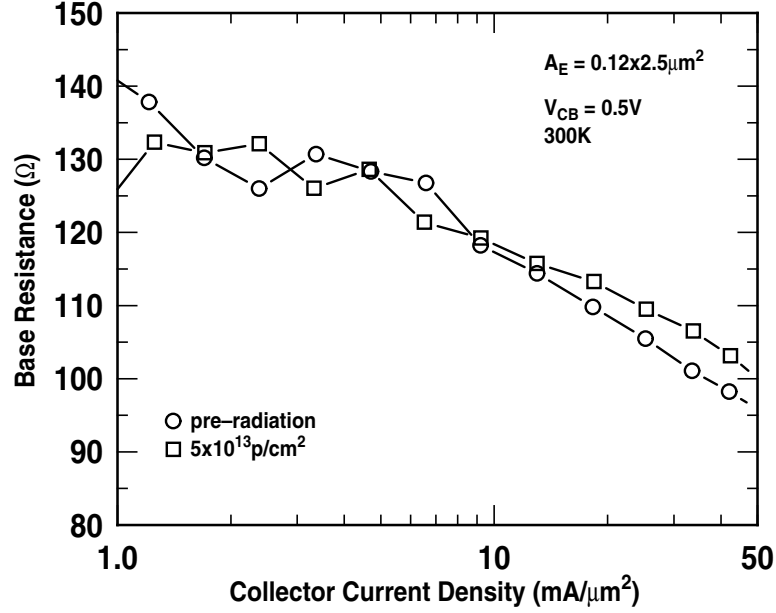


Figure 27: Pre- and post-radiation r_{bb} variation with J_C for 4th-generation SiGe HBTs.

to the fact that small-signal parameter extraction in this lower bias regime may be less accurate on account of the smaller dynamic range of the VNA and is therefore considered to be well within the range of measurement error. Finally, the forward emitter-collector transit time (τ_{EC}), as a function of proton fluence, for 2nd-, 3rd- and 4th-generation SiGe HBTs are illustrated in Figure 28. The vertical scaling methodologies outlined in [21] enables a further reduction in τ_{EC} to a record value of 0.45 psec, as shown in the Figure. More importantly, τ_{EC} remains remarkably independent of proton fluence up to an extreme level of $1 \times 10^{14} \text{ p/cm}^2$ in the case of the 3rd- and 4th-generation SiGe HBT-generation device. This is in stark contrast to the monotonic increasing relationship between τ_{EC} and fluence for the 2nd generation device, an indication that the new raised extrinsic base structure also affords carrier transit paths that are further removed from areas of high radiation induced trap density areas around the Si/SiO_2 interfaces.

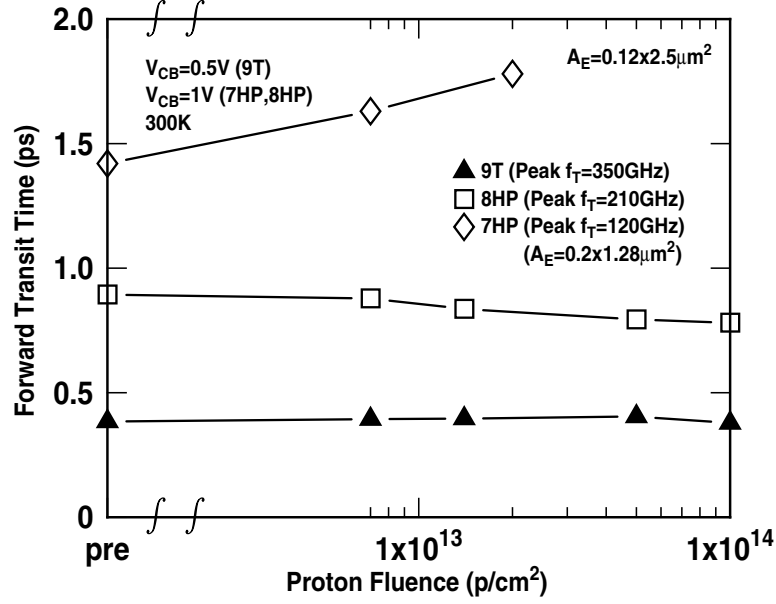


Figure 28: The τ_{EC} variation with fluence for 2nd-, 3rd- and 4th-generation SiGe HBTs.

3.5 Collector Doping

The ever increasing demands placed on device designers to realize transistors with higher operating frequencies and breakdown voltages, lower off-state leakage, reduced noise and smaller linewidths results in creative techniques to cater for certain applications. In this section devices with different N_C , used to tailor the breakdown voltage, are investigated.

Depending on the integration schemes, target applications and processing steps involved a variety of collector doping levels and methods may be chosen. In SiGe BiCMOS applications, for example, the n^+ sub-collector on a p^- substrate form the foundation for the npn transistor. From this base a high temperature epitaxial collector layer is grown to a thickness of approximately $(0.4 - 0.6 \mu m^2)$ and a doping of $5 \times 10^{15} cm^{-3}$. The collector epitaxial layer is contacted to the sub-collector via an implanted reach-through of sheet resistance near $10 - 20 \Omega m^2$. The high J_C performance and breakdown voltage of the device can be selectively tuned using a local collector implant close to the CB junction.

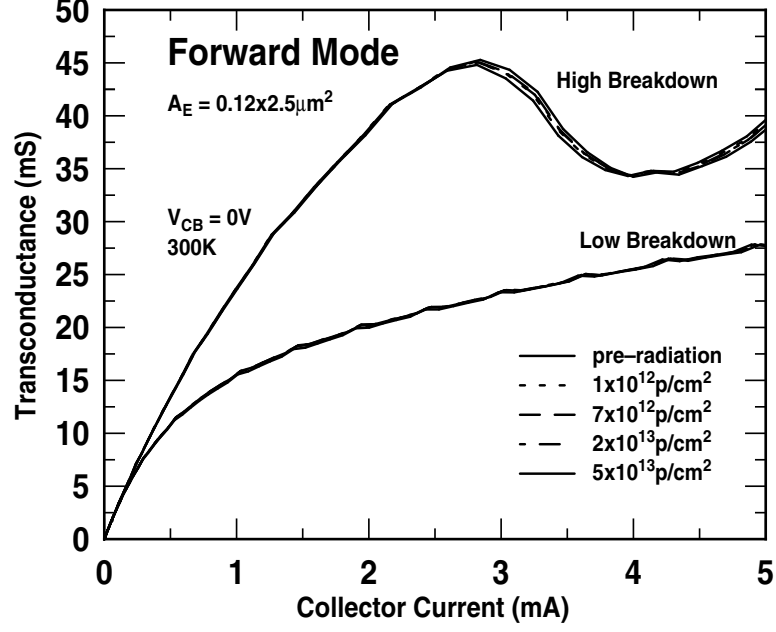


Figure 29: Extrinsic transconductance for the high- and low-breakdown devices (4th-generation).

A closer look at the inverse-mode I_B degradation of the 4th-generation, 350GHz SiGe HBTs shown in Figure 23 indicates that the low-breakdown transistors (with their higher N_C) are slightly more susceptible to proton induced damage at the CB junction than those with a higher-breakdown (lower N_C). In the low-breakdown device N_C is increased to delay the onset of high injection heterojunction barrier effects (HBE) and Kirk effect [67]. Typically, this yields an increased collector-base charge capacitance (C_{CB}) and avalanche multiplication ($M - 1$) that results in a reduced f_{max} and BV_{CEO} respectively [4]. However, careful collector profile optimization can be employed to simultaneously realize improvement in both f_T and BV_{CEO} [68, 69]. In the case of the devices under study, an increased N_C translates into a CB junction now pushed physically closer to the STI edge where the radiation induced G/R trap density is high. The extrinsic transconductance (g_m) of both high- and low-breakdown devices is shown in Figure 29. The onset of HBE clearly occurs at a much lower I_C than that of the low-breakdown device, a consequence of the lower N_C doping level in the high-breakdown device and

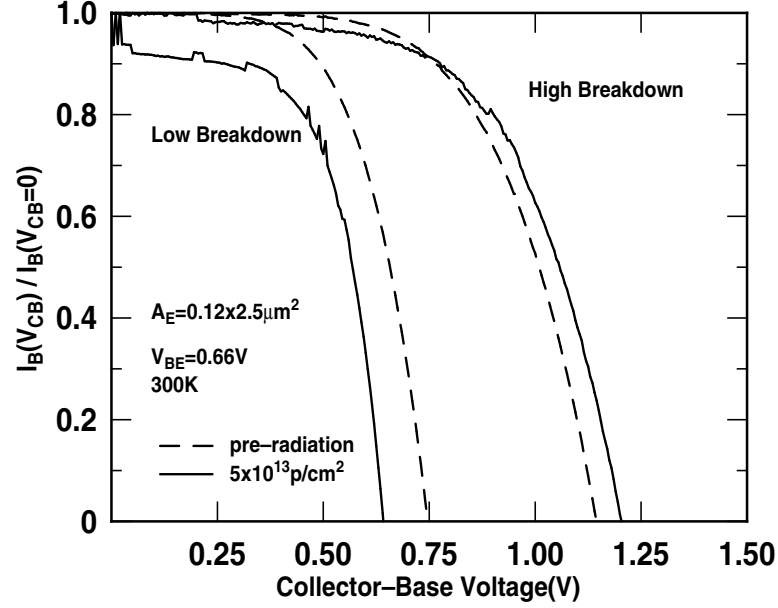


Figure 30: Neutral base recombination for the high- and low-breakdown devices (4th-generation).

in both cases, is insensitive to proton radiation, clearly good news from a circuit perspective.

The impact of irradiation on neutral base recombination (NBR) is shown in Figure 30 for $V_{BE} = 0.66V$. It is evident that the low-breakdown device, with its increased N_C , exhibits a much stronger post-radiation NBR component at low V_{CB} , as manifested by the increased $I_B(V_{CB})/I_B(0)$ factor. This is the result of increased recombination of minority and majority carriers in the base. Increased base-recombination results in an increase in I_B and reduction in β as observed in Figure 21. In the case of the high-breakdown device, the post radiation NBR component is significantly less. Figure 30 also demonstrates that the breakdown voltage, BV_{CEO} (extracted as the voltage at which $I_B(V_{CB})/I_B(0) = 0$) increases with fluence in the case of the high-breakdown device, but decreases in the case of the low-breakdown device. The low injection, forced- I_B output characteristics depicted in Figure 31 provide additional evidence of this result. The post-radiation output characteristics of the low-breakdown device demonstrate increased avalanche

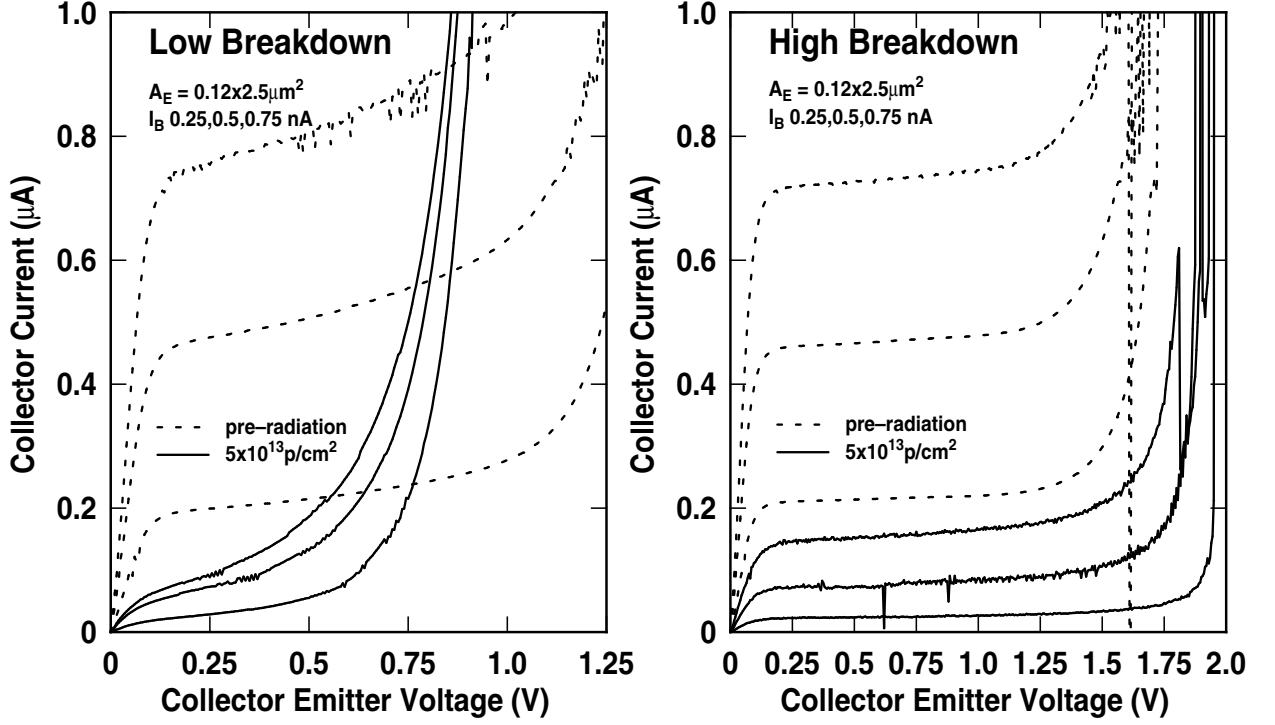


Figure 31: Forced I_B output characteristics for high- and low-breakdown devices(4th-generation).

multiplication, and a reduced V_A , BV_{CEO} , and β , whereas the results for the high-breakdown device indicate that these effects are not nearly as pronounced, and BV_{CEO} even *increases*. These results indicate again that strong electric fields, as reported in [52], this time in the CB junction (on account of high N_C), negatively impact the post-radiation device performance.

3.6 Summary

The proton tolerance of 4th-generation SiGe HBTs is assessed through critical analysis of the post-radiation effect on *ac* and *dc* Figures-of-merit. Specifically a moderate 6% decrease is observed for both f_T and f_{max} (well within the measurement error of the setup) and β at peak f_T experiences less than 0.3% reduction. Both forward and inverse I_B leakage for the 3rd- and 4th-generation devices are significantly lower than that of previous technology nodes, a testament to inherent resilience of the raised extrinsic base structure in improving the isolation of the EB

and CB junctions from radiation induced traps. Additionally, subtle differences in the response of 4th-generation devices with different collector doping have been explored. These results clearly indicate that SiGe HBTs continue to maintain excellent total dose tolerance in the midst of aggressive technology scaling.

CHAPTER IV

GAMMA AND PROTON DEGRADATION IN SIGE HBTs

4.1 Introduction

In this chapter, results for the ionization damage in 3rd generation SiGe HBTs due to gamma irradiation is presented. The previous chapter demonstrated that the proton tolerance of the technology was increased using the raised-extrinsic base structure which effectively resulted in a physical removal of the silicon-oxide interfaces (EB spacer, STI edge) from the EB and CB junctions respectively. In this chapter, comparisons are made between the 3rd and 2nd generation structures to assess the impact of the device cross section on the ionization only damage component of the observed total damage. Additionally, comparisons between the observed proton and gamma tolerance of the 3rd generation structures are made. Anomalous differences observed in these comparisons are paralleled to similar trends observed in proton irradiations of different dose rates. Finally, additional consideration is given to damage factor extractions and annealing characteristics.

4.2 Experiment Design

4.2.1 Devices under Test

The devices chosen to assess the impact of technology scaling on gamma-induced radiation include 2nd-generation (120GHz SiGe HBT) ($A_E = 0.2 \times 1.28\mu\text{m}^2$ and $0.2 \times 6.4\mu\text{m}^2$) and 3rd-generation (200GHz SiGe HBT) ($A_E = 0.12 \times 2.0\mu\text{m}^2$ and $0.12 \times 4.0\mu\text{m}^2$) samples irradiated simultaneously to facilitate unambiguous comparisons. A 200 GHz SiGe HBT (A_E of $0.12 \times 2.0\mu\text{m}^2$) was chosen as the primary device geometry of interest for comparing proton and gamma radiation damage. Additionally, devices of varying A_E were included to examine the geometrical dependencies of the observed post-radiation excess base-current density

$(\Delta J_B = J_B(post) - J_B(pre))$. Similar sample preparation techniques to those described in chapter 3 were used.

4.2.2 Test Facilities

Gamma irradiation was performed using a J.L. Shepard Model 81 Co-60 source at the Goddard Space Flight Center Radiation Effects Facility (GSFC REF). Dose rates varied from 20.5 to about 29.1 rad(Si)/sec. The dose was uniform to within 10% across all test samples, as determined using an ion chamber probe. In accordance with MIL-STD 883 Method 1019.6, a Pb/Al box was used to decrease the flux of secondary gamma and ensure a monochromatic gamma ray spectrum. All devices were irradiated with all terminals terminated inside of a black conductive foam resulting in a floating terminal condition during irradiation. Previous studies have revealed no significant differences in the response of SiGe HBTs to ionizing radiation for floating versus grounded pin configurations [61]. Total doses ranged from 92 krad(Si) to 3,792 krad(Si) and the samples were immediately measured after reaching the target gamma dose.

4.3 *dc Results*

Forward and inverse gummel measurements were used to facilitate a quantitative comparison of the radiation induced damage in 200GHz SiGe HBTs as a function of both proton and gamma irradiation. In the next sections several issues are considered including (i) technology scaling, (ii) proton and gamma comparisons, (iii) dose rate effects, (iv) damage factor extraction and (v) annealing.

4.3.1 Technology Scaling and Gamma Degradation

The forward- and inverse-mode mode Gummel characteristics of the 200GHz SiGe HBT ($0.12 \times 2.0 \mu\text{m}^2$) are depicted in Figures 32 and 33 as a function of the cumulative gamma dose up to 3.3Mrad. As has been observed with proton irradiation, the characteristic increase in the low-injection base current density

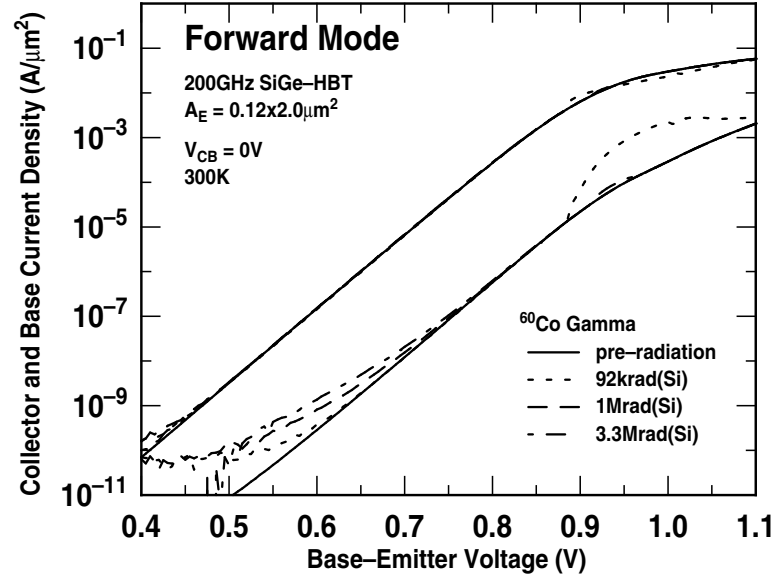


Figure 32: Forward-mode 200GHz SiGe HBT gummel characteristics as a function of cumulative gamma dose.

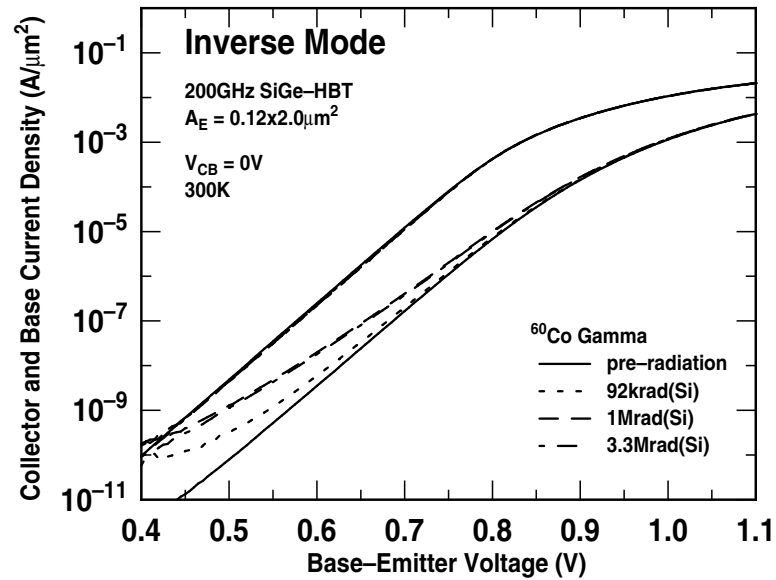


Figure 33: Inverse-mode 200GHz SiGe HBT gummel characteristics as a function of cumulative gamma dose.

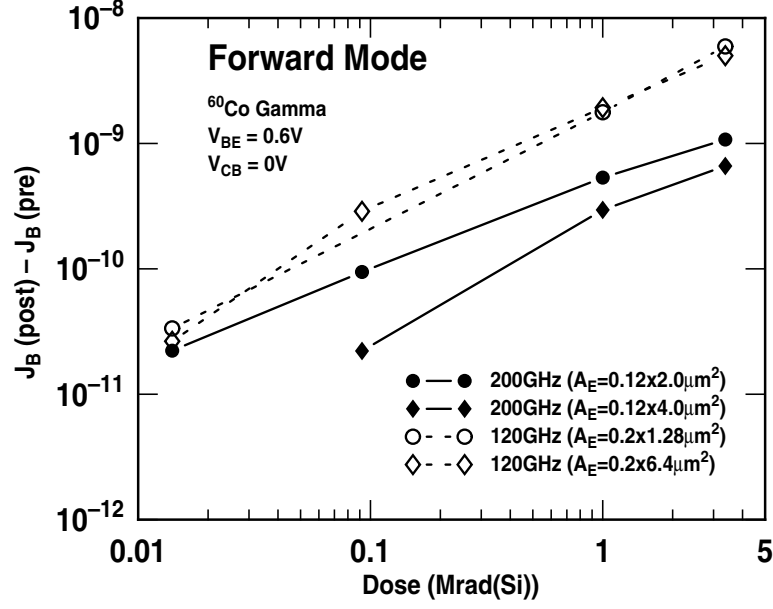


Figure 34: Forward-mode excess base current density as a function of gamma dose.

($J_B = I_B/A_E$) is clearly evident in both plots. As has been well documented in the literature [64], this phenomenon is the result of radiation-induced generation-recombination (G/R) traps near the EB spacer (forward-mode) and STI (inverse-mode) silicon-oxide interface regions. The forward and inverse mode ΔJ_B , as well as the normalized peak current-gain ($\beta_{peak(post)}/\beta_{peak(pre)}$) are used to quantify the effects of technology scaling (120GHz and 200GHz SiGe HBTs) on observed gamma degradation (as was done for protons). The 200GHz SiGe HBT is shown to have a reduced forward-mode ΔJ_B as depicted in Figure 34. A similar trend for the proton response was observed, as shown in chapter 3, and has been attributed to the novel raised extrinsic base structure yielding EB junctions physically further removed from the EB spacer oxide. Additionally, the 200GHz SiGe HBTs exhibit a ΔJ_B that has a stronger functional dependence on A_E than for the 120GHz devices. In the case of the 200GHz SiGe HBT, the inverse-mode ΔJ_B , illustrated in Figure 35 is an order of magnitude higher than its forward-mode counterpart, indicating that gamma radiation results in more damage in the CB junction for these devices. This is in direct contrast to the 120GHz SiGe HBTs,

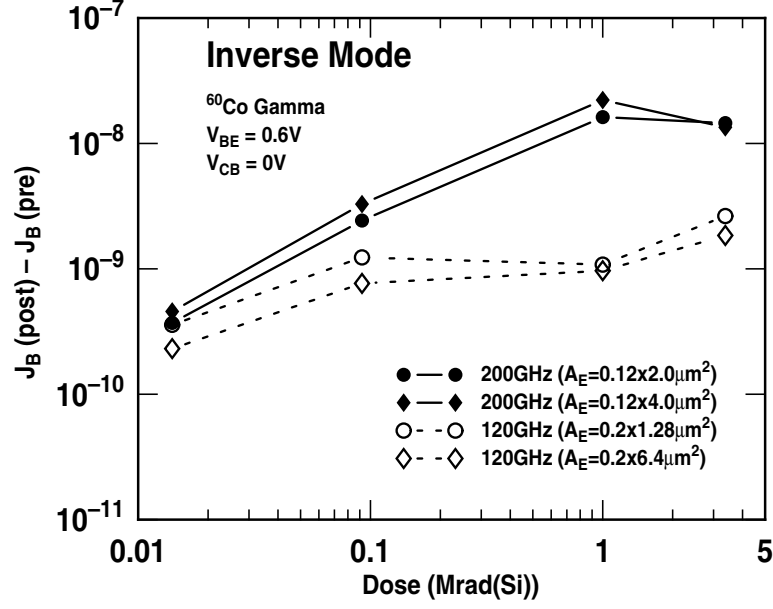


Figure 35: Inverse-mode excess base current density as a function of gamma dose.

where the damage is comparable at both junctions. This difference between the inverse mode characteristics of the 120 GHz and 200 GHz devices is qualitatively consistent with the use of a slightly thicker oxide in the STI region for the 200GHz transistors. The STI processing conditions (i.e., interfacial properties) was similar for both technologies [20, 25].

4.3.2 Proton vs. Gamma Comparison

The post-radiation forward and inverse ΔJ_B calculated from in-situ measurements of both the proton and gamma irradiation experiments are compared in this section. Ionization damage is a dominant mechanism in both, however protons are able to generate additional displacement damage. In this section, the comparisons are facilitated using 200GHz SiGe HBTs of varying A_E . The forward and inverse mode results are depicted in Figures 36 and 38.

The forward mode ΔJ_B follows a weak power law dependence when plotted on a semilog graph as a function of the equivalent cumulative gamma dose. This is particularly more pronounced for protons than for gamma. It is also observed

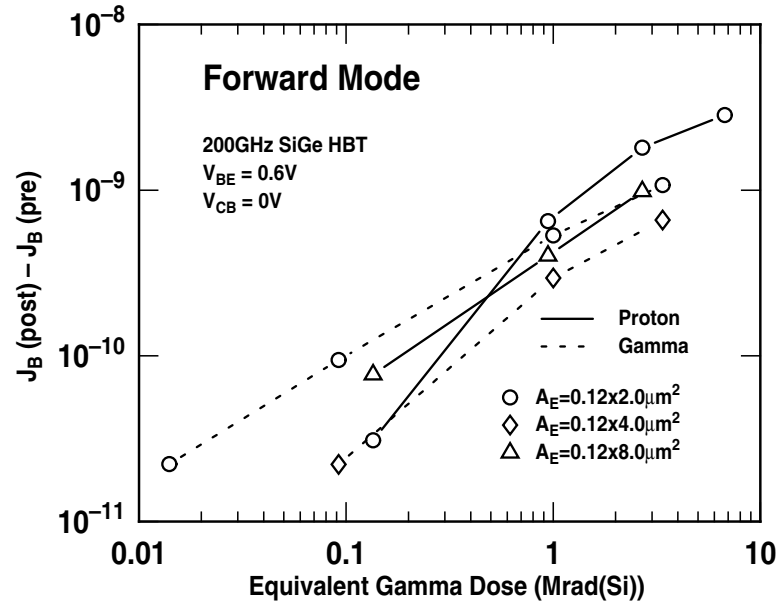


Figure 36: Forward-mode excess base current density for both protons and gamma irradiation in 200GHz SiGe HBTs plotted as a function of equivalent gamma dose.

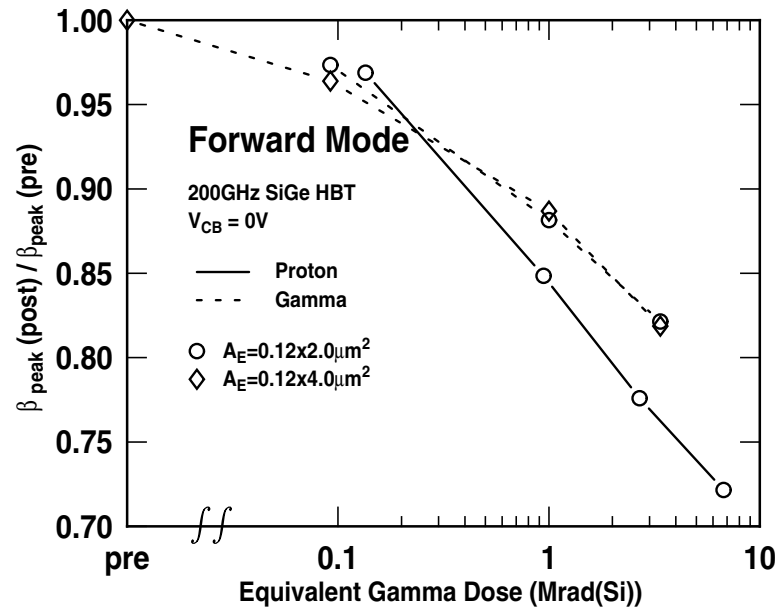


Figure 37: Forward-mode peak current gain degradation for both protons and gamma irradiation in 200GHz SiGe HBTs plotted as a function of equivalent gamma dose.

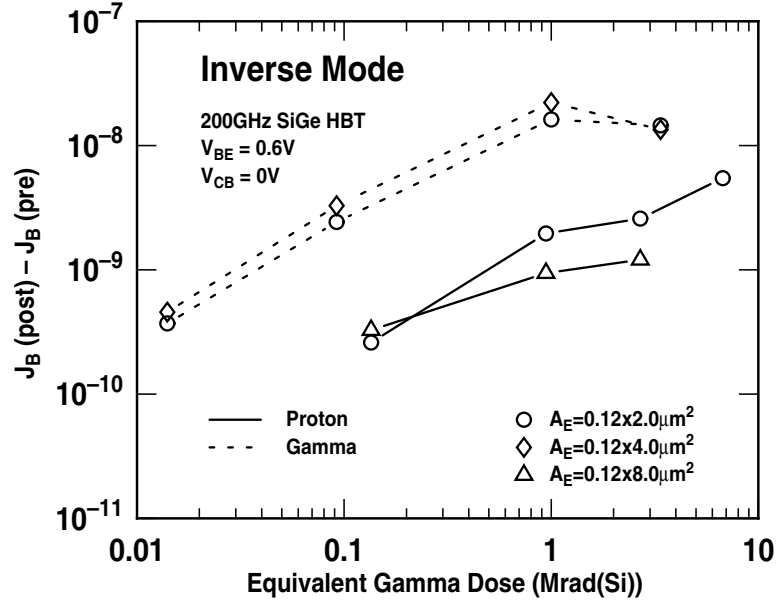


Figure 38: Inverse-mode excess base current density for both protons and gamma irradiation in 200GHz SiGe HBTs plotted as a function of equivalent gamma dose.

that the protons show an increased degradation when compared to gamma, as is expected, especially at the higher dose levels ($> 1 \text{ Mrad}$). The forward-mode peak β degradation as a function of cumulative dose is illustrated in Figure 37 and is consistent with the results depicted in Figure 36, particularly at higher doses.

More importantly, although the inverse mode ΔJ_B exhibits the same functional form, it is observed that the gamma degradation is consistently at least one order of magnitude higher than that of the corresponding proton irradiation. This is a very significant result since it has conventionally been expected that protons, which are able to cause both displacement and ionization damage would be able to generate more traps in the bulk region of the device closer to the STI oxides. This would perturb the transport dynamics near the CB junction of the device and would be manifested as increased inverse mode ΔJ_B .

It should also be noted that a simple minor error in dosimetry cannot explain these results, since the observed differences are quite large. Moreover, this anomalous trend has been observed in multiple samples, and has been previously demonstrated in experiments performed on 1st generation SiGe HBTs for gamma

[74] and proton irradiation [64]. This difference between protons and gamma for forward versus inverse mode is an unexpected result, and has important implications for radiation hardness assurance. One possible explanation of these results is that the differences in the dose rates of proton and gamma irradiation dominates the damage mechanism. ELDRS, (Enhanced Low Dose Rate Studies) effects for ionizing radiation on SiGe HBTs have been very well documented, but such results have been conventionally obtained in SiGe HBTs using gamma irradiation [75].

4.4 Dose Rate Effects

4.4.1 Review of Dose Rate Effects for Ionizing Radiation

The increased radiation induced degradation for low-dose-rate ionizing irradiations has been studied extensively. Known as the "Enhanced Low Dose Rate Sensitivity, this phenomenon was first discovered for bipolar transistors in 1991 by Enlow et al. [76]. In that study, polysilicon and crystalline emitter BJTs underwent gamma irradiation at dose rates from 1.1rad/s to 300rad/s. The reciprocal change in current gain, $\frac{1}{\Delta\beta}$, was used as the Figure of merit. For the polysilicon transistor $\frac{1}{\Delta\beta}$ was an order of magnitude higher for the 1.1rad/s dose rate. Additional work on the ELDRS effect was next performed in 1994 by Fleetwood et al. [77]. In this effort, MOS capacitors were fabricated in an effort to simulate the fields near Si/SiO_2 interfaces associated with the EB spacer and STI oxides. Gamma irradiations at 0V bias and at room temperature yielded significant shifts in the midgap capacitance-voltage characteristic for the low-dose rate (25 – 40% for $10rad(SiO_2)/s$) compared to the high-dose rate (10% for $100rad(SiO_2)/s$). It was inferred that such a shift is the result of an increase in the positive-oxide-trapped charge (N_{ox}), previously determined to be a key damage mechanism [78] as described in chapter 2. Additionally, it was inferred that such a shift was enough to explain the enhanced degradation in the Si BJTs on account of the exponential dependance of I_B on N_{ox} .

Dose rate effects for SiGe HBTs was next performed by Banerjee et al. [75]. In these studies, devices were exposed to 1.43MeV Cobalt-60 sources up to a cumulative dose of 50krad(Si) at dose rates of $0.1\text{rad}(\text{Si})/\text{s}$ and $300\text{rad}(\text{Si})/\text{s}$. The results from this study indicated that the observed dose rate effects were highly technology dependent and varied significantly depending on the regime over which dose rates were chosen, the technology being irradiated and the source of radiation. Specifically, it was determined that SiGe HBTs exhibited minimal dose rate dependence over the $0.1\text{rad}(\text{Si})/\text{s}$ to $300\text{rad}(\text{Si})/\text{s}$ range, especially when compared to the results from Nowlin et al [79]. To be sure some technologies proved to be sensitive only down to $10\text{rad}(\text{SiO}_2)/\text{s}$ [79] while other experiments yielded dose-rate sensitivities even down to $0.005\text{rad}(\text{SiO}_2)/\text{s}$ [80]. Additionally, for SiGe HBTs an initial *decrease* in I_B at low V_{BE} was observed up to a cumulative dose of $5\text{krad}(\text{Si})$ for a dose rate of $0.1\text{rad}(\text{Si})/\text{s}$, followed by a subsequent *increase* in I_B for the same dose-rate for total doses in excess of $5\text{krad}(\text{Si})$. The proposed mechanism for the observed anomalies derived using 2D MEDICI simulations involved the gamma induced annealing of pre-existing radiation traps N_T from near midgap, to a more shallow level, thereby resulting in a reduction in the I_B .

There are still several open issues on the ELDRS topic. Several physical mechanisms have been proposed in attempts to explain the observed effects. Pershenkov et al. [81] demonstrated that the emitter-base junction bias is extremely influential in the low-dose rate transistor response. Transistors biased in the forward mode exhibited an enhancement of the dose rate effect by a factor of 1.5 for *npn* and 3 for *pnp* devices for ionizing radiation using Cr/Y and X-ray sources. Another model involving the interaction of fringing electric fields at the screen oxide was proposed to account for the experimental observations. The presence of shallow electron traps in the bulk oxides was proposed as another damage mechanism by the same group [82] in a study concentrating on MOSFETs. Dose-rate effects are a logical underlying factor behind the anomalous results observed in the prior section in which proton and gamma irradiations are observed to have different

Table 6: Incremental dose rate comparison for the proton and gamma irradiation of 200GHz SiGe HBTs

Proton		Gamma	
Dose ($rad(Si)$)	Rate ($rad(Si)/s$)	Dose ($rad(Si)$)	Rate ($rad(Si)/s$)
135×10^3	918	14×10^3	15
808×10^3	1.942×10^3	78×10^3	20
1.756×10^6	1.883×10^3	960×10^3	1.0×10^3
4.053×10^6	1.829×10^3	2.31×10^6	1.750×10^3
Proton Total: 6.73Mrad		Gamma Total: 3.36Mrad	

effects on the collector-base and emitter-base junctions for forward and inverse mode. In an effort to investigate this a dose-rate study for proton irradiations was performed on the 200GHz SiGe HBTs. The results are presented in the next section.

4.4.2 Proton Dose Rate Effects in SiGe HBTs

As previously discussed, several practical considerations must be made when performing irradiation experiments. Among these are cost, time, beam current, dose rate and health physics to name a few. For in-situ measurements it is often the case that the dose rate in between steps are not identical. Table 6 illustrates some of the typical dose rates for the proton and gamma studies described thus far. In the above table the incremental steps for proton irradiation are described in terms of their equivalent gamma dose determined from dosimetry measurements. Immediately it is clear that for low cumulative doses ($< 100krad(Si)$) there are at least two orders of magnitude difference between the dose rates for proton ($1.942 \times 10^3 rad(Si)/s$) and gamma ($20 rad(Si)/s$) irradiation. These results indicate that it is possible that an underlying dose rate mechanism could be responsible for the anomalous results observed for gamma irradiation in the inverse mode.

In an effort to further address the observed differences between the proton and gamma irradiation results a proton dose rate investigation was performed. 200GHz SiGe HBTs of varying A_E were each irradiated up to a cumulative fluence of 1Mrad at dose rates of $30 rad(Si)/s$, $100 rad(Si)/s$, $300 rad(Si)/s$ and $1krad(Si)/s$.

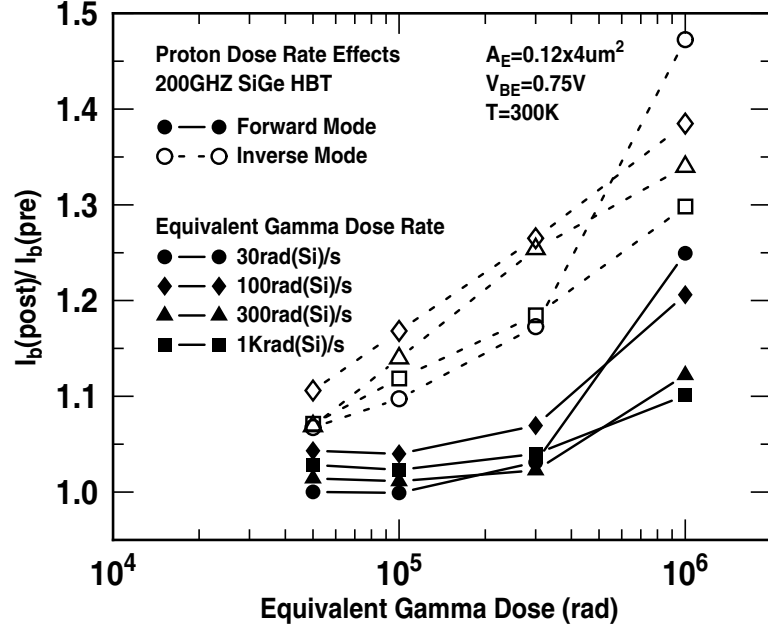


Figure 39: Forward and inverse mode base current density for a 200GHz SiGe HBT showing proton dose rate effects.

Forward and inverse gummel in-situ measurements were then taken at 50krad, 100krad, 300krad and 1Mrad. The results are displayed in Figures 39-40. The above Figures indicate that there is indeed increased radiation induced degradation for lower proton dose rates observed at a $V_{BE} = 0.75V$ for a 200GHz SiGe HBT with an emitter area $A_E = 0.12 \times 4.0 \mu m^2$. This is reminiscent of the ELDRS effect documented in the literature [76]. It should be noted that at other bias levels, such a dependence is less obvious as has been previously demonstrated [75]. In Figure 39, the lower dose-rate samples exhibit increased post-radiation base current density ratios ($\left(\frac{I_{B,post}}{I_{B,pre}}\right)$). These trends are more pronounced as the total dose tends toward 1Mrad. The post radiation excess base current density ($J_{B,post} - J_{B,pre}$) is plotted in Figure 40 and clearly shows an increased inverse mode ΔJ_B compared to the forward mode. The differences in dose rates are less evident in this plot.

The degradation from proton dose rate tests is then compared with conventional proton and gamma irradiations previously discussed. These are depicted

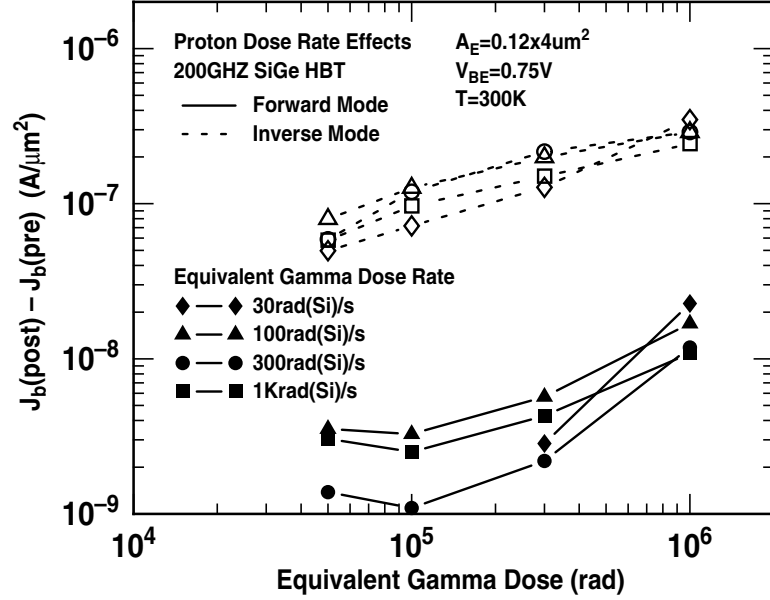


Figure 40: Forward and inverse mode excess base current for a 200GHz SiGe HBT showing proton dose rate effects.

in Figures 41 and 42 overlaid with the current proton dose rate results. It is clearly evident that the differences in the proton and gamma irradiation that were observed in the inverse mode can, to some extent, be reproduced via proton irradiations of different dose rates. As depicted in Table 6 there are significant differences in the dose rates of the proton and gamma samples which may be responsible for some of the observed anomalies. This result suggests that in addition to competing displacement damage versus ionizing radiation effects, there is also an underlying dose rate factor involved. The proton dose rate study was performed on devices of varying emitter areas ($A_E = 0.12\mu\text{m}^2, 0.24\mu\text{m}^2, 0.48\mu\text{m}^2$ and $0.96\mu\text{m}^2$) with all devices exhibiting similar trends as depicted in Figure 43. In order to further address the sensitivity of these 200GHz SiGe HBTs dose rate comparisons for gamma sources is currently under investigation.

4.5 Damage Factor Extraction

Damage coefficients are often a convenient way to quantify the extent of radiation damage in a material exposed to several different particle types. To be sure,

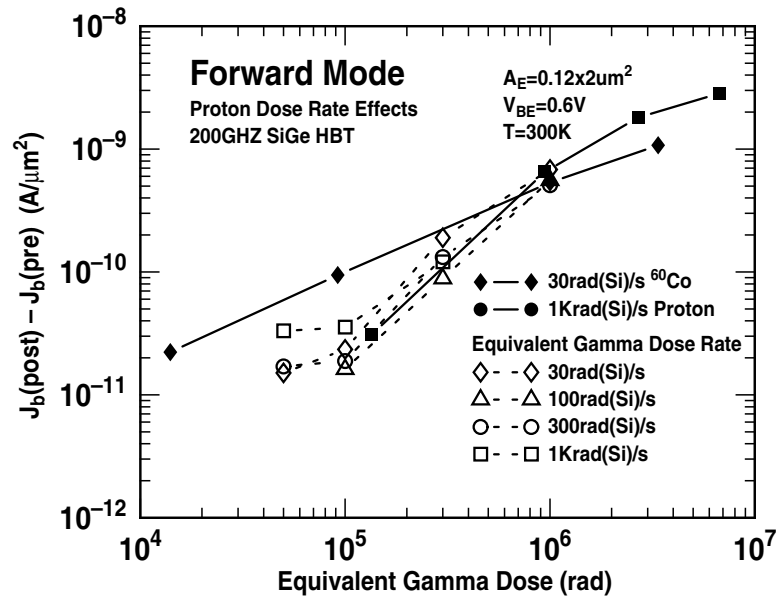


Figure 41: Forward mode excess base current for a 200GHz SiGe HBT showing proton dose rate effects compared to standard proton and gamma irradiations.

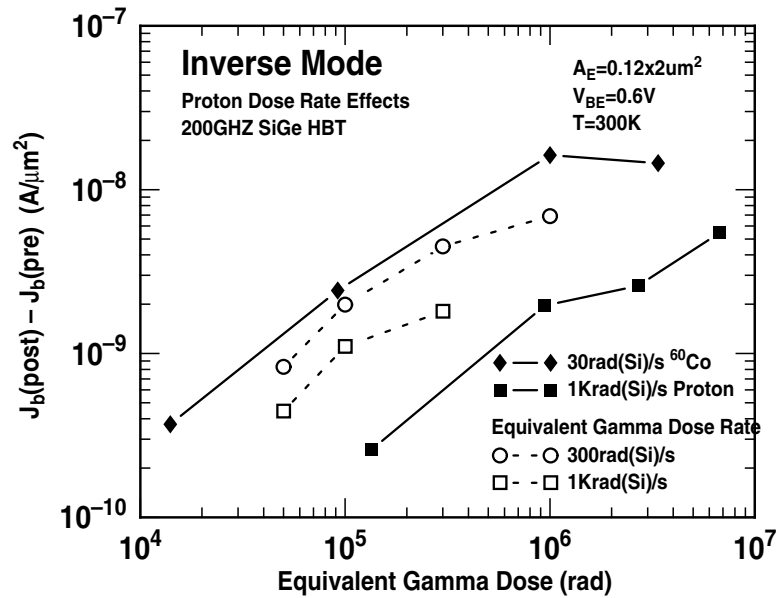


Figure 42: Inverse mode excess base current for a 200GHz SiGe HBT showing proton dose rate effects compared to standard proton and gamma irradiations.

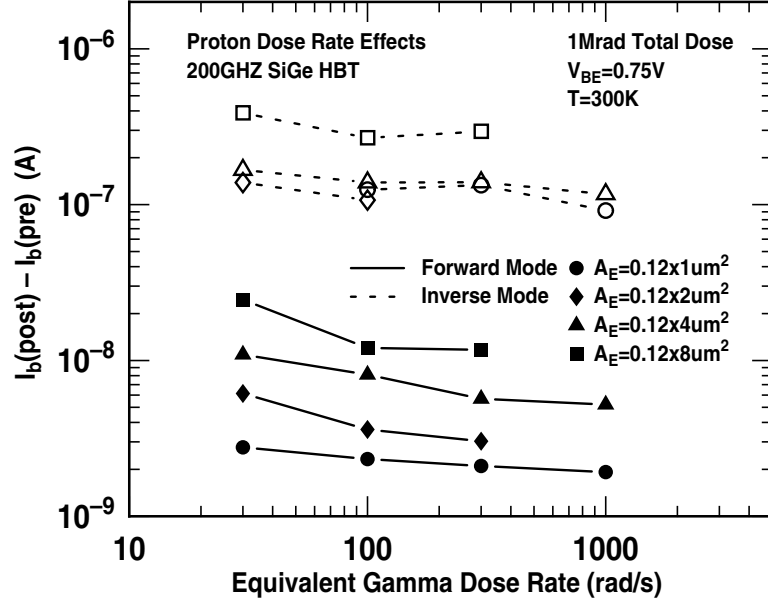


Figure 43: Forward and inverse mode excess base current density as a function of dose rate for devices of varying emitter areas.

damage coefficients depend on the particle type and energy, material type and resistivity, impurity species and concentration as well as the injection level, temperature and time after irradiation [35]. In this section we compute the damage factors for proton and gamma irradiation. Protons can cause both displacement and ionization damage, as a result of this the reciprocal gain is only linear over a finite range [4]. To extract the damage factor, $K(E, \phi)$ the reciprocal current gain, $\beta^{-1}(\phi)$, is plotted as a function of dose $rad(Si)$ for different J_C . Next, a first order linear fit is performed and the data extrapolated to the range of proton fluence, ϕ . A similar plot is made for $\beta^{-1}(\phi)$ this time as a function of ϕ from a proton irradiation experiment. Finally, the slopes of the extrapolated data and the proton irradiation data are subtracted from each other to yield K_E . Therefore, one needs both gamma and proton irradiations for the above computation. According to the method outlined above, the displacement damage factor $K(E, \phi)$ for the medium energy (63MeV) of chapter 3. The Messenger-Spratt equation [70], defines the functional relationship between $\beta^{-1}(\phi)$ and $K(E, \phi)$ as depicted in Equation 41. Although the original work performed by Messenger et al, focused

Table 7: Forward and Inverse Gamma Displacement Damage Factors for 120GHz and 200GHz SiGe HBTs

$f_T(\text{GHz})$	$A_E(\mu\text{m}^2)$	Gamma $K(E, \phi) \text{ cm}^2/p$	
		Forward	Inverse
200	0.12x2.0	1.96×10^{-17}	4.43×10^{-16}
	0.12x4.0	1.36×10^{-17}	4.06×10^{-16}
120	0.2×1.28	1.61×10^{-16}	1.48×10^{-16}
	0.2×6.4	1.89×10^{-16}	1.43×10^{-16}

Table 8: Forward and Inverse Proton Displacement Damage Factors for 200GHz SiGe HBTs

$f_T(\text{GHz})$	$A_E(\mu\text{m}^2)$	Proton $K(E, \phi) \text{ cm}^2/p$	
		Forward	Inverse
200	0.12x2.0	2.32×10^{-16}	2.72×10^{-16}
	0.12x4.0	3.20×10^{-16}	

on displacement damage effects of neutrons on Si and Ge, Equation. 41 has been successfully used by others in the calculation of damage factors for neutrons, protons, α -particles, deuterons and electrons [71, 72] .

$$K(E, \phi) = \frac{1}{\beta(\phi)} - \frac{1}{\beta_0} \quad (41)$$

The results of these calculations, for forward-mode degradation, are displayed in Tables 7 and 8. Calculations are based on the $\beta^{-1}(\phi)$ degradation at $J_C = 1 \mu\text{A}/\mu\text{m}^2$.

In the forward mode, the calculated $K(E, \phi)$ values are in the range of 10^{-16} and are about three orders of magnitude less than those calculated for 1st generation 50GHz SiGe HBTs [73] for 63MeV proton irradiation. Moreover, the 200GHz devices exhibit a proton $K(E, \phi)$ that is an order of magnitude larger than that for gamma, indicative of a larger proportion of displacement damage related effects during proton exposure, as expected. Finally, as is observed in proton irradiation, the gamma $K(E, \phi)$ for 200GHz SiGe HBTs is also an order of magnitude less than that for 120GHz SiGe HBTs. These results are in agreement with the observed transistor-level trends in forward-mode post-radiation ΔJ_B and β degradation. The

calculated inverse-mode gamma damage factors $K(E, \phi)$ are approximately that of the corresponding forward mode values. The larger inverse-mode degradation (compared to forward-mode) for gamma irradiation is consistent with observed results for 50GHz SiGe HBTs as was seen in [74] with exactly the opposite effect also seen for proton irradiation [74] which indicates that even in this new 3rd generation structure gamma irradiation induces a larger trap density near the STI region.

4.5.1 Annealing

4.5.1.1 Annealing Theory

Device level metrics (such as ΔJ_B) are observed to decrease when the device is re-measured post radiation. Annealing trends for devices subject to displacement damage are evident when the device is left at (i) room temperature (self-annealing), (ii) after the perturbation of carrier densities (injection-annealing) or after being subjected to elevated temperatures (thermal-annealing) [33]. Studies of neutron irradiation experiments on bulk Si devices have resulted in the definition of short term or transient annealing (complete within hours) and long term, more stable anneals that occur over several days. Short term annealing phenomena has been attributed to defect re-ordering immediately after an irradiation event, long-term annealing is typically characterized via measurements at a fixed temperature as a function of time (isothermal), or alternatively as a function of temperature for a fixed time (isochronal) [33]. High temperature annealing experiments have been performed on the 200GHz SiGe HBTs, the results of which are described in the next section.

4.5.2 Isothermal Annealing in SiGe HBTs

Proton and gamma irradiated 200GHz SiGe HBTs were annealed at $T_A = 300^\circ\text{C}$ for varying time steps t_a using the AET Rapid Thermal Annealing system. The chamber was first purged with 2sccm of N_2 for a total of two minutes. Next the

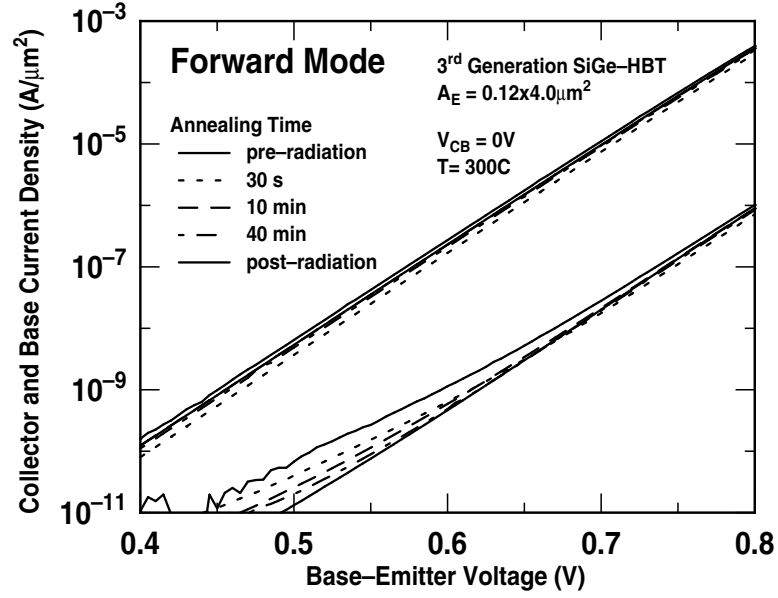


Figure 44: Reduction in the forward-mode post radiation base current leakage as a function of anneal time at 300C.

ambient gas was switched to forming gas (N_2H_2) and the temperature ramped to T_A at a rate of $100C/min$. The furnace was then held at the specified anneal temperature $T_A = 300C$ for the anneal time t_a . At the end of the anneal, the high temperature lamps are switched off and the devices are left to cool. In this regime there is an exponential decrease in temperature with time. Once the temperature has gotten to $100C$ the devices are removed. The entire anneal is performed at atmospheric pressure and in forming gas. Following the anneal, samples were remeasured and then annealed again for another length of time at the same temperature. It should be noted that these samples were annealed at high temperature after a significant period of room temperature self annealing for both proton (3months) and gamma (6months) annealing. It should be noted that there is still considerable damage after room temperature annealing. The forward and inverse mode gummel characteristics, measured as a function of annealing time for post-radiation gamma irradiated samples, are depicted in Figures 44 and Figures 45 respectively. The monotonic reduction in the post radiation J_B as a function of the annealing time is clearly evident and is indicative of an annealing

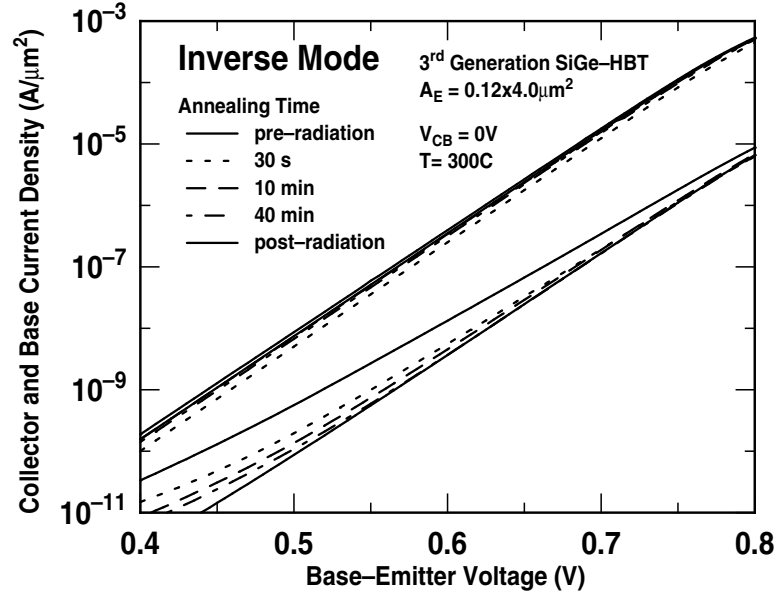


Figure 45: Reduction in the inverse-mode post radiation base current leakage as a function of anneal time at 300C.

of damage possibly caused by the migration of radiation induced trap states (E_T) from the midgap ($E_G/2$) to more shallow levels.

The base current ratio for annealed and post-radiation samples are compared for both proton and gamma irradiation for several device geometries. The forward and inverse mode results are illustrated in Figures 46 and 47 respectively. In the forward mode, the geometrical dependence is clearly evident. Devices with larger A_E have previously been shown to exhibit increased degradation due to an increased perimeter for the Si/SiO_2 interface around the EB spacer. Figure 46 clearly shows that the largest A_E has the lowest post-anneal base current ratio, both for room temperature self anneal, and high temperature anneal increments. Additionally, in the forward mode, proton irradiated device exhibit a greater percentage decrease in the post-anneal base current ratio when compared to gamma irradiated devices both annealed over the same time period. This can possibly be explained by the fact that the proton irradiated devices have had less time to self anneal, however, closer inspection of Figure 47 indicates that there is a fundamental physical mechanism behind these observations. As is

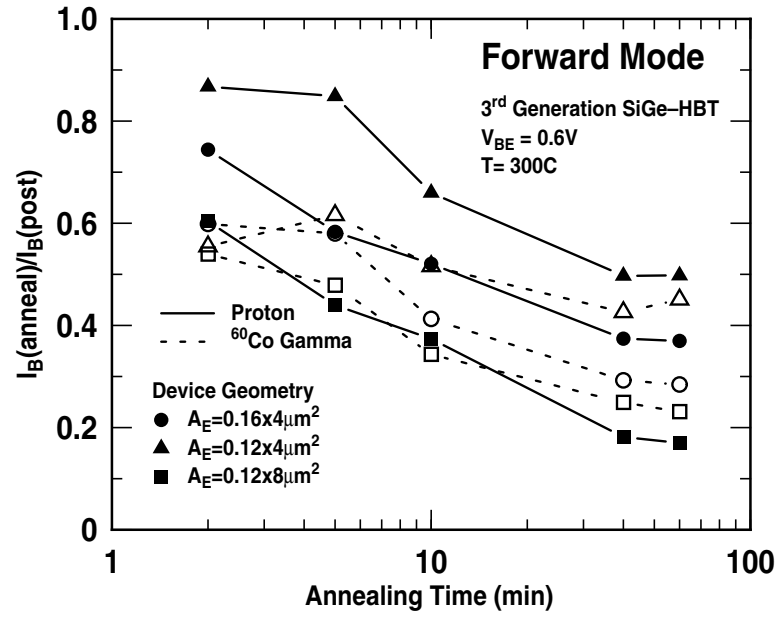


Figure 46: Ratio of the post-anneal base current to post-radiation base current in the forward mode for different annealing time steps at 300C.

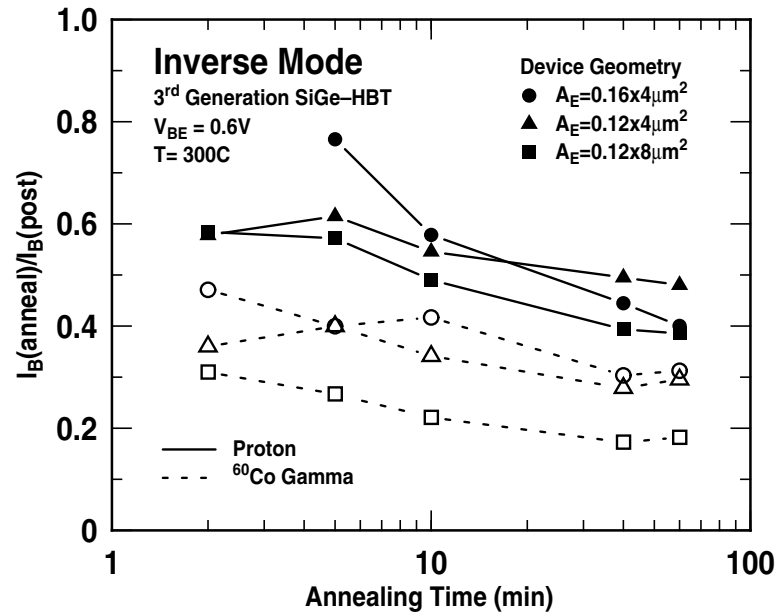


Figure 47: Ratio of the post-anneal base current to post-radiation base current in the inverse mode for different annealing time steps at 300C

expected and evident in Figure 47, in the inverse mode there is no functional dependence of the device geometry on the radiation induced damage or the post-anneal base current ratio. More importantly however, unlike the trends observed in the forward mode, the annealing of the proton and gamma irradiated devices exhibit very similar gradients when plotted as post-anneal base current ratio as a function of time. This result, along with the others already outlined, indicate that there is something different between the trap dynamics of proton and gamma formed at the EB and STI oxides.

4.6 *Summary*

In this section, gamma-degradation of 200GHz SiGe HBTs has been presented. The influence of technology scaling and device geometry on the observed response was quantitatively assessed and comparisons were made to previously proton radiation results. The 200GHz SiGe HBTs exhibited a significantly reduced forward-mode peak β degradation and ΔJ_B when compared to 120GHz SiGe HBTs. Similar trends were observed for proton- and gamma-induced degradation. The inverse mode gamma ΔJ_B , however, is an order of magnitude higher than for protons. The calculated proton displacement damage factors for the 200GHz SiGe HBTs are three orders of magnitude less than those of their 50GHz counterparts, and one order of magnitude less than that calculated for 200GHz devices under gamma irradiation. Inverse-mode damage factors are approximately twice the forward-mode value for gamma irradiation, but approximately the same for protons. These results are consistent with those observed for 1st generation 50GHz SiGe HBTs. Additional proton dose rate experiments performed to further probe these anomalies indicate that a similar enhanced degradation at low proton dose rates is present. The high temperature annealing behavior has also been presented.

CHAPTER V

CONCLUSION

In this chapter, the contributions to the body of literature on radiation effects in advanced bipolar devices will be outlined. Also, areas of interest for future study will be discussed.

5.1 Topical Review

The purpose of this work was to investigate the proton and gamma tolerance of advanced 3rd-generation 200GHz Silicon-Germanium Heterojunction Bipolar Transistors (SiGe HBTs).

In chapter I, background information on SiGe HBTs was provided. The commercial relevance of SiGe BiCMOS technology in the extra terrestrial telecommunications industry was cited as the principal driving factor behind interest in its radiation response. The fabrication techniques, and physical mechanisms behind the device operation were described next. Finally an overview of the trends in technology scaling over the past decade was described using industry examples from IBM microelectronics.

Chapter II presented a fundamental description of the relevant aspects of radiation physics as it applies to its interaction with semiconductor materials. Radiation environments are described in terms of their nomenclature and particle types, with particular emphasis on space radiation environments encountered by satellites in orbit around the earth. Next, displacement damage mechanisms in silicon and silicon-germanium are described. Ionization damage mechanisms in semiconductors are also described with particular emphasis on photon and heavy charge particle interaction with matter.

The proton tolerance of 200GHz SiGe HBTs were described in chapter III. A comprehensive analysis of the effects of technology scaling on radiation-induced degradation demonstrated that the novel raised-extrinsic base structures employed yielded emitter-base and collector-base junctions that are physically further removed from the high trap density oxide interfaces yielding the device more tolerant to high levels of ionizing dose. As discovered in the previous technology generations, negligible changes in the *ac* characteristics were observed. Process splits used to produce high- and low-breakdown transistors were also investigated and it was determined that the increased collector doping used in the low-breakdown devices resulted in enhanced degradation when compared to the high-breakdown devices with lower collector doping.

In chapter IV the gamma tolerance of 200GHz SiGe HBTs were investigated. Comparisons gamma degradation for both 200GHz and 120GHz devices demonstrated that the raised extrinsic base structure yields improved tolerance to ionizing radiation. Proton and gamma degradation comparisons revealed that in the forward-mode devices were more susceptible to proton damage, however, in the inverse-mode the devices were more susceptible to gamma damage. These anomalous results were also discovered for 1st-generation SiGe HBTs and confirmed by damage factor calculations. Additional experiments with different proton dose rates were performed and used to support the theory that the vastly different dose rates between the proton and gamma irradiation experiments may be the cause of an underlying dose rate effect responsible for the observed results.

5.2 Future Direction

Several of the empirical results described in the work have been explained via very plausible physical mechanisms based on literature reviews. In order to facilitate a more complete understanding however, the observed results need to be understood via an accurate quasi-3D device simulation. In particular the differences in the response of the high- and low-breakdown to proton radiation,

the variation in the observed response in the forward- and inverse-mode with the emitter-spacer perimeter and shallow trench isolation perimeter respectively need to be understood.

Additionally, in an effort to further understand the proton dose rate effects, and the anomalous differences between the proton and gamma degradation in the forward and inverse mode, additional gamma dose rate experiments are needed.

Finally, further understanding of the fundamental differences between the displacement and ionization damage of these devices will be better understood through a comparison of displacement-only particles (such as neutrons) with the observed gamma degradation. From a hardness assurance perspective, protons have traditionally been used as they are thought to represent the worst case (ionization+displacement) damage scenario.

REFERENCES

- [1] Technology Industry Association, *2005 Telecommunications Market Review and Forecast*, Available online at <http://www.tiaonline.org/media/mrf/>.
- [2] P. Marshall and C. Marshall, "Proton effects and test issues for satellite designers - Part A: Ionization effects," Short Course Notes, *IEEE Nuclear Space and Radiation Effects Conference.*, 1999.
- [3] C. Marshall and P. Marshall, "Proton effects and test issues for satellite designers - Part B: Displacement effects," Short Course Notes, *IEEE Nuclear Space and Radiation Effects Conference.*, 1999.
- [4] J.D. Cressler and G. Niu, *Silicon-Germanium Heterojunction Bipolar Transistors*, Artech House, Boston, 2003.
- [5] Y. Lu, J.D. Cressler, R. Krithivasan, Y. Li, R.A. Reed, P.W. Marshall, C. Polar, G. Freeman, and D. Ahlgren, "Proton Tolerance of a Third Generation, 0.12 μm 185 GHz SiGe HBT Technology," *IEEE Transactions on Nuclear Science*, vol. 50, pp. 1811-1815, Dec 2003.
- [6] P.W. Marshall, M.A. Carts, A. Campbell, D. McMorro, S. Buchner, R. Stewart, B. Randall, B. Gilbert, R.A. Reed, "Single event effects in circuit hardened SiGe HBTs at gigabit per second data rates," *IEEE Transactions on Nuclear Science*, vol. 47, pp. 2669-2674, Dec 2000.
- [7] R.F. Pierret, *Semiconductor Device Fundamentals*, Addison-Wesley, Redding, 1996.
- [8] D.L. Hareme, B.S. Meyerson "The Early History of IBM's SiGe Mixed Signal Technology," *IEEE Transactions on Electron Devices*, vol. 48, pp. 2555-2565, Nov 2001.
- [9] S.A. Campbell, *The Science and Engineering of Microelectronic Fabrication* Oxford University Press, New York, 2001.
- [10] E. Kasper and F. Schaffler, Group IV compounds, *Semiconductors and Semimetals*, Ed. T.P. Pearsall (Academic Press 1991), vol. 33, pp 223-309, 1991.
- [11] S.C. Jain, R. Bullough, and J. Willis, A review of theoretical and experimental work on the structure of $\text{Ge}_x\text{Si}_{1-x}$ strained layers and superlattices, *Advanced Physics* vol. 39, pp. 127-90, 1990.
- [12] M. Matura, J.M. Tonnerre and G.S. Cargill, Lattice parameters and local atomic structure of silicon rich SiGe/Si(100) films, *Physics Review B* vol. 44, pp. 3842-9, 1991.
- [13] L. Geppert, 'The Amazing Vanishing Transistor Act,' *IEEE Spectrum*, October, 2002, pp. 28-33.

- [14] S.C. Jain *Germanium-Silicon Strained Layers and Heterostructures* Academic Press, San Diego, 1994.
- [15] A. Fischer, H.-J. Osten, and H. Richter, "An equilibrium model for buried SiGe strained layers", *Solid State Electronics*, vol.44, pp.869-873, 2000.
- [16] R.B. Herring, L.P. Hunt, W.C. O'Mara *Handbook of Semiconductor Silicon Technology*. Park Ridge, NJ: Noyes, 1990.
- [17] B.S. Meyerson, "Low-temperature Si and SiGe epitaxy by ultrahigh-vacuum/chemical vapor deposition: Process fundamentals," *IBM Journal of Research and Development*, vol. 34, no. 6, pp. 132-141, 1990.
- [18] J.D. Cressler, "SiGe HBT Technology: A New Contender for Si-Based RF and Microwave Circuit Applications", *IEEE Transactions on Microwave Theory and Techniques*, March, 1998, pp. 572-589.
- [19] D.C. Ahlgren, G. Freeman, S. Subbanna, R. Groves, D. Greenberg, J. Malinowski, D. Nguyen-Ngoc, S.J. Jeng, K. Stein, K. Schonenberg, D. Kiesling, B. Martin, S. Wu, D.L. Harame, B. Meyerson "A SiGe HBT BiCMOS technology for mixed signal RF applications," *Proceedings of the IEEE Bipolar/BiCMOS Circuits Technology Meeting*, pp. 195-198, 1997.
- [20] A. Joseph, D. Coolbaugh, M. Zierak, R. Wuthrich, P. Geiss, Z. He, X. Liu, B. Orner, J. Johnson, G. Freeman, D. Ahlgren, B. Jagannathan, L. Lanzerotti, V. Ramchandran, J. Malinowski, H. Chen, J. Chu, P. Gray, R. Johnson, J. Dunn, S. Subbanna, K. Schonenberg, D. Harame, R. Groves, K. Watson, D. Jadus, M. Meghelli, and A. Rylyakov "A $0.18\mu\text{m}^2$ BiCMOS technology featuring a 120/100 GHz (f_T/f_{max}) HBT and ASIC-compatible CMOS using copper interconnect," *Proceedings of the IEEE Bipolar/BiCMOS Circuits Technology Meeting*, pp. 143 - 146, 2001.
- [21] J.-S. Rieh, B. Jagannathan, H. Chen, K.T. Schonenberg, D. Angell, A. Chinthakindi, J. Florkey, F. Golan, D. Greenberg, S. -J. Jeng, M. Khater, F. Pagette, C. Schnabel, P. Smith, A. Stricker, K. Vaed, R. Volant, D. Ahlgren, G. Freeman, K. Stein, and S. Subbanna, "SiGe HBTs with Cut-off Frequency of 350GHz," in *Technical Digest IEEE International Electron Devices Meeting*, pp. 771-774, 2002.
- [22] J.-S. Rieh, D. Greenberg, M. Khater, K.T. Schonenberg, S. -J. Jeng, F. Pagette, T. Adam, A. Chinthakindi, J. Florkey, B. Jagannathan, J. Johnson, R. Krishnasamy, D. Sanderson, C. Schnabel, P. Smith, A. Stricker, S. Sweeney, K. Vaed, T. Yanagisawa, D. Ahlgren, K. Stein, and G. Freeman, "SiGe HBTs for Millimeter-Wave Applications with Simultaneously Optimized f_T and f_{max} of 300GHz" in *Technical Digest IEEE Radio Frequency Integrated Circuits Symposium*, pp. 395-398, 2004.
- [23] M. Khater, J.-S. Rieh, T. Adam, A. Chinthakindi, J. Johnson, R. Krishnasamy, M. Meghelli, F. Pagette, D. Sanderson, C. Schnabel, K.T. Schonenberg, P. Smith, K. Stein, A. Stricker, S.-J. Jeng, D. Ahlgren, and G. Freeman "SiGe HBT Technology with f_T/f_{max} =350/300GHz and gate delay below 3.3ps," in *Technical Digest IEEE International Electron Devices Meeting*, pp. 247-250, 2004.

- [24] E. O. Johnson, "Physical limitations on frequency and power parameters of transistors," *RCA Review*, vol. 26, pp. 163-177, 1965.
- [25] B. Jagannathan, M. Khater, F. Pagette, J.-S. Rieh, D. Angell, H. Chen, J. Florkey, F. Golan, D. R. Greenberg, R. Groves, S. J. Jeng, J. Johnson, E. Mengistu, K.T. Schonenberg, C.M. Schnabel, P. Smith, A. Stricker, D. Ahlgren, G. Freeman, K. Stein, and S. Subbanna, "Self-Aligned SiGe NPN Transistors With 285 GHz f_{max} and 207 GHz f_T in a Manufacturable Technology," *IEEE Electron Device Letters*, vol. 23, pp. 258-260, May 2002.
- [26] H. Kroemer "Two integral relations pertaining to electron transport through a bipolar transistor with a nonuniform energy gap in the base region," *Solid State Electronics*, vol. 28, pp. 1101-1103, 1985.
- [27] P. Marmier, and E. Sheldon, *Physics of Nuclei and Particles*, Volume I, Academic Press, New York, 1969.
- [28] C. Claeys and E. Simoen, *Radiation Effects in Advanced Semiconductor Materials and Devices*, Springer-Verlag, Berlin, 2002.
- [29] NASA Space Environments and Effects (SEE) Program "Technical Working Group-Ionosphere and Thermosphere," available online at <http://see.msfc.nasa.gov/pf/pf.htm>
- [30] E.G Stassinopolous, G.J Brucker, D.W. Nakamura, C.A. Stauffer, G.B. Gee, and J.L. Barth, "Solar flare proton evaluation at geostationary orbits for engineering applications," *IEEE Transactions on Nuclear Science*, vol. 43, pp. 369-382, 1996.
- [31] A Holmes-Siedle and L. Adams, *Handbook of radiation effects*, Oxford University Press, Oxford, 1993.
- [32] F. Larin, *Radiation Effects in Semiconductor Devices*, John Wiley and Sons, New York, 1968.
- [33] J.R. Srouf, C.J. Marshall, P.W. Marshall, "Review of displacement damage effects in silicon devices," *IEEE Transactions on Nuclear Science*, vol. 50, pp. 653-670, June 2003.
- [34] A.S. Grove *Physics and Technology of Semiconductor Devices*, Wiley, New York, 1967.
- [35] J.R. Srouf, D.M. Long, D.G. Millward, R.L. Fitzwilliam, and W.L. Chadsey *Radiation Effects on and Dose Enhancement of Electronic Materials*, Noyes Publications, Parkridge, 1984.
- [36] D.V. Lang "Deep level transient spectroscopy: A new method to characterize traps in semiconductors" *Journal of Applied Physics* vol.45, pp.3023-3032, 1974.
- [37] A. Hallen, N. Keskitalo, F. Masszi, and V. Nagl "Lifetime in proton irradiated silicon" *Journal of Applied Physics* vol.79, pp.3906-3914, 1996.

- [38] H. Bleichner, P. Jonsson, N. Keskitalo, and E. Nordlander "Temperature and injection dependence of the Shockley-Read-Hall lifetime in electron irradiated n-type silicon" *Journal of Applied Physics* vol.79, pp.9142-9148, 1996.
- [39] N. Keskitalo, P. Jonsson, K. Nordgren, H. Bleichner, and E. Nordlander "Temperature and injection dependence of the Shockley-Read-Hall lifetime in electron irradiated p-type silicon" *Journal of Applied Physics* vol.83, pp.4206-4212, 1998.
- [40] G.D. Watkins "Intrinsic defects in silicon" *Materials Science in Semiconductor Processing* vol.3, pp.227-235, 2000.
- [41] C.V. Budtz-Jorgensen, P. Kringhoj, A.L. Nylansted, and N.V. Abrosimov "Deep level transient spectroscopy of the Ge-vacancy pair in Ge-doped n-type silicon" *Physics Review B* vol. 58, pp.1110-1113, 1998.
- [42] , A. Kawasuso, M. Suezawa, S. Okada, T. Honda, and I. Yonenaga, "Positron annihilation study of electron-irradiated Si_xGe_{1-x} bulk crystal" *Journal of Applied Physics* vol.81, pp.2916-2918, 1997.
- [43] P. Kringhoj and A.L. Nylandseted, "Irradiation-induced defect states in epitaxial n-type $Si_{1-x}Ge_x$ alloy layers" *Physics Review B* vol.52, pp.16333-16336, 1995.
- [44] E.V. Monakhov, A.L. Nylandsted, and P. Kringhoj, "Electron defect levels in relaxed epitaxial p-type $Si_{1-x}Ge_x$ layers produced by MeV proton irradiation" *Journal of Applied Physics* vol.81, pp.1180-1183, 1997.
- [45] J. Wesler, J.L. Hoyt, and J.F. Gibbons "NMOS and PMOS transistors fabricated in strained silicon/relaxed silicon-germanium structures" *Technical Digest IEEE International Electron Devices Meeting*, pp.1000-1002, 1992.
- [46] T. Ghani, M. Armstrong, C. Auth, M. Bost, P. Charvat, G. Glass, T. Hoffmann, K. Johnson, C. Kenyon, J. Klaus, B. McIntyre, K. Mistry, A. Murthy, J. Sandford, M. Silberstein, S. Sivakumar, P. Smith, K. Zawadzki, S. Thompson and M. Bohr "A 90nm high volume manufacturing logic technology featuring novel 45nm gate length strained silicon CMOS transistors" *Technical Digest IEEE International Electron Devices Meeting*, pp. 978-980, 2003.
- [47] S.A. Goodman, F.D. Aurret, K. Nauka, and J.B. Malherbe, "Defect characterization of n-type $Si_{1-x}Ge_x$ after 1.0keV helium-ion etching" *Journal of Elecron Materials* vol.26, pp.463-469, 1997.
- [48] H. Ohyama, J. Vanhellemont, Y. Takami, K. Hayama, H. Sunaga, J. Poortmans, M. Caymax, and P. Clauws, "Germanium content dependence of radiation damage in strained $Si_{1-x}Ge_x$ epitaxial devices" *IEEE Transactions on Nuclear Science* vol.41, pp.2437-2442, 1994.
- [49] H. Ohyama, J. Vanhellemont, Y. Takami, K. Hayama, H. Sunaga, J. Poortmans, and M. Caymax, "Degradation of $Si_{1-x}Ge_x$ epitaxial heterojunction bipolar transistors by 1-MeV fast neutrons" *IEEE Transactions on Nuclear Science* vol.42, pp.1550-1557, 1995.

- [50] H. Ohyama, K. Hayama, J. Vanhellemont, J. Poortmans, M. Caymax, Y. Takami, H. Sunaga, I. Nashiyama, and Y. Uwakoto "Degradation of $Si_{1-x}Ge_x$ epitaxial devices by proton irradiation" *Applied Physics Letters* vol.69, pp.2429-2431, 1996.
- [51] H. Ohyama, J. Vanhellemont, Y. Takami, K. Hayama, H. Sunaga, I. Nashiyama, Y. Uwakoto, J. Poortmans, and M. Caymax, "Degradation and recovery of proton irradiated $Si_{1-x}Ge_x$ epitaxial devices" *IEEE Transactions on Nuclear Science* vol.43, pp.3089-3096, 1996.
- [52] J.D. Cressler, M.C. Hamilton, G.S. Mullinax, Y. Li, G. Niu, C.J. Marshall, P.W. Marshall, H.S. Kim, M.J. Palmer, A.J. Joseph, and G. Freeman, "The Effects of proton Irradiation on the Lateral and Vertical Scaling of UHV/CVD SiGe HBT BiCMOS Technology," *IEEE Transactions on Nuclear Science*, vol. 47, pp. 2515-2520, Dec 2000.
- [53] F.B. McLean, T.R. Oldham, "Basic mechanisms of radiation effects in electronic materials and devices," *US Army Lab Command, HDL-TR-2129* . US Army Command, Harry Diamond Laboratories, MD, USA 1987.
- [54] John Lilley, *Nuclear Physics: Principles and Applications* John Wiley and Sons, Chichester, 2001.
- [55] E. Rutherford, "The scattering of α and β particles by matter and the structure of the atom" *Philosophy Magazine* vol.21, pp.699, 1911.
- [56] H. Geiger and E. Marsden, "On the diffuse reflection of the α particles" *Proceedings of the Royal Society of London* vol.82, pp. 495, 1909.
- [57] H. Geiger, "The scattering of α -particles by matter" *Proceedings of the Royal Society of London* vol.83, pp.492, 1910.
- [58] F.B. McClean, H.E. Boesch, Jr., and T.R. Oldham, "Electron-hole generation, transport and trapping in SiO_2 " *Ionizing Radiation Effects in MOS Devices and Circuits* Wiley, New York, 1989.
- [59] K.M. Murray, W.J. Stapor, and C. Casteneda, "Calibrated charged particle radiation system with precision dosimetric measurement and control," *Nuclear Instruments and Methods in Physics Research*, vol. A281, pp.616-621, Sept 1989.
- [60] P.W. Marshall, C.J. Dale, M.A. Carts, and K.A. Label, "Particle-induced bit errors in high performance fiber optic data links for satellite data management," *IEEE Transactions on Nuclear Science*, vol. 41, pp. 1958-1965, Dec 1994.
- [61] S.Zhang, J.D. Cressler, G. Niu, C.J. Marshall, P.W. Marshall, H.S. Kim, R.A. Reed, M.J. Palmer, A.J. Joseph, and D.L. Harame, "The effects of operating bias conditions on the proton tolerance of SiGe HBTs" *Solid State Electronics*, vol. 47, pp. 1729-1734, 2003.
- [62] C. Grens, "The effects of operating bias conditions on the proton tolerance of SiGe HBTs" *Solid State Electronics*, vol. 47, pp. 1729-1734, 2003.

- [63] S.Zhang, G. Niu, J.D. Cressler, S.D. Clark, and D.C. Ahlgren, "The effects of proton irradiation on the RF performance of SiGe HBTs," *IEEE Transactions on Nuclear Science*, vol. 46, pp. 1716-1721, 1999.
- [64] J.D. Cressler, R. Krithivasan, G. Zhang, G. Niu, P.W. Marshall, H.S. Kim, R.A. Reed, M.J. Palmer, and A.J. Josephy, "An investigation of the origins of the variable proton tolerance in multiple SiGe HBT BiCMOS technology generations," *IEEE Transactions on Nuclear Science*, vol. 49, pp. 3203-3207, 2002.
- [65] A.H. Johnston, R.E. Plaag, "Models for total dose deradation of linear integrated circuits", *IEEE Transactions on Nuclear Science*, vol 34, pp.1474-1480, 1987.
- [66] S.J. Mason, "Power gain in feedback amplifiers" *IRE Transactions on Circuit Theory*, vol. CT-1, pp. 20-25, 1954.
- [67] C.T. Kirk "Theory of transistor cutoff frequency falloff at high current densities" *IRE Transactions on Electron Devices*, vol. 3, pp. 164-170, 1964.
- [68] B.G. Malm, T. Johansson, T. Arnborg, H. Norstrom, J.V. Grahn, M. Ostling, "Implanted collector profile optimization in a SiGe HBT process," *Solid State Electronics*, vol. 45, pp. 399-404, March 2001.
- [69] A.J. Joseph, J.D. Cressler, D.M. Richey, G. Niu "Optimization of SiGe HBTs for operation at high current densities," *IEEE Transactions on Electron Devices*, vol. 46, pp. 1347-1354, July 1999.
- [70] G.C. Messenger and J.P. Spratt "The effects of neutron irradiation on silicon and germanium" *Proceedings of the IRE*, vol. 46, pp 1038-1044, 1958.
- [71] G.P. Summers, C.J. dale, E.A. Burke, E.A. Wolicki, P.W. Marshall, and M.A. Gehlhausen "Correlation of particle-induced displacement damage in silicon" *IEEE Transactions on Nuclear Science* vol.34, pp. 1134-1139, 1987.
- [72] C.J. Dale, P.W. Marshall, E.A. Burke, G.P. Summers, and E.A. Wolicki "High energy electron induced displacement damage in silicon" *IEEE Transactions on Nuclear Science* vol.35, pp. 1208-1214, 1988.
- [73] S.Zhang, J.D. Cressler, S. Subbanna, R. Groves, G. Niu, T Isaacs-Smith, J. Williams, H. Bakhru, P.W. Marshall, H.S. Kim, and R.A. Reed "An investigation of proton energy effects in SiGe HBT technology" *IEEE Transactions on Nuclear Science*, vol. 49, pp. 3208-3212, 2002.
- [74] J.D. Cressler, R. Krithivasan, A.K. Sutton, J.E. Seler, J.F. Kreig, S.D. Clark, and A.J. Joseph "The impact of gamma irradiation on SiGe HBTs operating at cryogenic temperatures" *IEEE Transactions on Nuclear Science*, vol. 50, pp. 1805-1810, 2003.
- [75] G. Banerjee, G. Niu, J.D. Cressler, S.D. Clark, M.J. Palmer, and D.C. Ahlgren "Anomalous Dose Rate Effects in Gamma Irradiated SiGe Heterojunction Bipolar Transistors" *IEEE Transactions on Nuclear Devices*, vol. 46, pp. 1620 - 1627, 1999.

- [76] E.W. Enlow, R.L. Pease, W. Combs, R.D. Schrimpf, and R.N. Nowlin "Response of Bipolar Processes to Ionizing Radiation" *IEEE Transactions on Nuclear Devices*, vol. 38, pp. 1342-1341, 1991.
- [77] D.M. Fleetwood, S.L. Koiser, R.N. Nowlin, R.D. Schrimpf, R.A. Reber Jr, M. DeLaus, P.S. Winokur, A. Wei, W.E. Combs, and R.L. Pease "Physical mechanisms contributing to enhanced bipolar gain degradation at low dose rates." *IEEE Transactions on Nuclear Science* vol. 41, pp. 1871-1883, 1994.
- [78] T.R. Oldham, F.B. McLean, H.E. Boesch, and J.M. McGarrity "An overview of radiation-induced interface traps in MOS structures" *Semiconductor Science and Technology* vol. 4, pp 986-999, 1989.
- [79] R.N. Nowlin, D.M. Fleetwood, and R.D. Schrimpf "Saturation of the dose-rate response of bipolar transistors below 10rad(SiO_2)/s: implications for hardness assurance" *IEEE Transactions on Nuclear Science* vol. 41, pp. 1637-1641.
- [80] S.C. Witczak, R.D. Schrimpf, D.M. Fleetwood, K.F. Galloway, R.C. Lacoe, D.C. Mayer, J.M. Puhl, R.L. Pease, and J.S. Suehle "Hardness assurance testing of bipolar junction transistors at elevated irradiation temperatures" *IEEE Transactions on Nuclear Science* vol. 44, pp. 1989-2000, 1997.
- [81] V.S. Pershenkov, V.B. Maslov, S.V. Cherepko, I.N. Shvetzov-Shilovsky, V.V. Belyakov, A.V. Sogoyan, V.I. Rusanovsky, V.N. Ulimov, V.V. Emelianov, and V.S. Nasibullin "The effect of emitter junction bias on the low dose rate radiation response of bipolar devices" *IEEE Transactions on Nuclear Science* vol. 44, pp. 1840 - 1848, 1997.
- [82] V.V. Belyakov, V.S. Pershenkov, A.V. Shalnov, and I.N. Shvetzov-Shilovsky, "Use of MOS structures for the investigation of low-dose-rate effects in bipolar transistors" *IEEE Transactions on Nuclear Science* vol. 42, pp. 1660 - 1666, 1995.